ARTICLES

Negative pion absorption at rest in ^{3}He

D. Gotta,* M. Dörr, † W. Fetscher,‡ G. Schmidt,§ and H. Ullrich
Kernforschungszentrum Karlsruhe, Institut für Kernphysik and Institut für Experimentelle Kernphysik, Universität Karlsruhe, D-76021 Karlsruhe, Germany

G. Backenstoss, M. Izycki,‖ W. Kowald, I. Schwanner, P. Weber,‡ and H. J. Weyer
Institut für Physik, Universität Basel, Klingelbergstrasse 82, CH-4056 Basel, Switzerland
(Received 3 June 1994)

The *pnn* and *dn* final states after the absorption of stopped pions in ^{3}He have been measured in a kinematically complete experiment covering the whole phase space. Proton-neutron, deuteron-neutron, and neutron-neutron coincidences have been detected with a charged-particle hodoscope and large-area time-of-flight counters. For the first time, triple coincidences between the pionic K x-rays and two particles have been measured thus selecting absorption from the atomic $1s$ state. It has been found that the absorption is dominated by the two-nucleon mechanism (2NA) on isoscalar nucleon pairs as indicated by the measured ratio of 6.3 ± 1.1 for back-to-back correlated *nn* and *pn* pairs. A substantial amount of the three-body final state *pnn* is affected by the final-state interaction (FSI) or leads to the two-particle final state *dn*. Ratios of 3.1 ± 0.4 for 2NA to FSI and of 4.2 ± 0.6 for the *pnn* to the *dn* final state are measured. No evidence has been found for three-nucleon absorption with an upper limit of $3\%/\pi^-_{\text{stop}}$.

PACS number(s): 25.80.Ls, 36.10.−k, 21.30.+y

I. INTRODUCTION

In the last decade, considerable progress has been made in the understanding of the basic reaction mechanism of pion absorption. The absorption on isoscalar spin-triplet nucleon-nucleon pairs has been studied in detail by means of the $\pi d \leftrightarrow NN$ reactions. In the context of the two-nucleon mechanism, the three-nucleon system ^{3}He has played a crucial role in these investigations because it is (besides ^{3}H) the simplest nucleus with more than two nucleons. With a probability of $\approx 90\%$, the nucleon pairs are in the relative states $^3S_1$ or $^1S_0$. Thus, the ^{3}He nucleus also allows reactions like two-nucleon absorption on an isovector proton-proton pair and all reactions with three nucleons participating in the absorption. Experimentally, the detection of two outgoing nucleons in coincidence permits a kinematically complete determination of the three-nucleon final state.

Pion absorption has been studied with pions in flight as well as with pions at rest. Comprehensive and detailed reviews have been given by Hüfner [1], Ashery and Schiffer [2], Ericson and Weise [3], and Weyer [4]. For in-flight measurements, p-wave pion absorption on isoscalar nucleon-nucleon pairs dominates the cross section [5–8]. The s wave is restricted to weaker channels like the absorption on isovector nucleon-nucleon pairs. The knowledge of the reaction mechanisms at zero energy is indispensable for a thorough understanding of pion absorption. The s-wave absorption can be studied better at rest because for pion absorption in flight, $\Delta(1232)$-isobar excitation dominates.

At rest, pion absorption takes place from well-defined states of a pionic atom. In the lightest nuclei such as ^{3}He, this orbit is an s state in most of the cases. The possibility of absorption from atomic p states complicates the situation. However, information about the relative contribution of s states is available from measurements of the pionic x-ray cascade. Exclusive absorption from the atomic $1s$ state can be selected by requiring a threefold coincidence between a K x-ray from the pionic ^{3}He atom and two outgoing particles in coincidence. This has been done in the present experiment.

On pion absorption at rest in ^{3}He, several investigations have been reported [9–11]. It is known that about $\frac{2}{3}$ of all pions captured in the pionic atom lead to the true absorption final states

$$\pi^-_{\text{stop}}\,{}^3\text{He} \rightarrow dn\ , \tag{1}$$

$$\pi^-_{\text{stop}}\,{}^3\text{He} \rightarrow pnn\ . \tag{2}$$

From the observation of charged particles, branching ratios of $(16 \pm 2)\%$ [9,10] and $(58 \pm 5)\%$ [9] were obtained for the channels *dn* and *pnn*, respectively. The sum of these two channels was measured indirectly to be $(68.2 \pm 2.6)\%$

*Institut für Kernphysik, Forschungszentrum Jülich, D-52425 Jülich, Germany.
†Bruker Physik, D-76189 Karlsruhe, Germany.
‡Institut für Teilchenphysik, ETH Zürich, CH-5232 Villigen, Switzerland.
§TÜV Bayern Sachsen, D-80686 München, Germany.
‖Université de Genève, Institut de Physique (D.P.N.C), 32 Bd. d'Yvoy, CH-1211 Genève 4, Switzerland.

[12] as complement of all the other possible decay channels:

$$\pi^-_{\text{stop}}\,{}^3\text{He} \rightarrow \pi^0 t\ , \tag{3}$$

$$\pi^-_{\text{stop}}\,{}^3\text{He} \rightarrow \gamma t,\ \gamma dn,\ \gamma pnn\ . \tag{4}$$

Charge exchange (3) and radiative capture (4) have been investigated in detail by various groups experimentally as well as theoretically and will not be considered in the present paper. An overview can be found in [13,14].

The main goal of this experiment is to identify the various channels which lead to the three-body final state *pnn* (2). The following four channels have to be considered: (2a) isoscalar pair absorption on ${}^3S_1$ proton-neutron pairs with one proton as spectator (2NA), (2b) isovector pair absorption on ${}^1S_0$ proton-proton or proton-neutron pairs with the neutron or one proton as spectator (2NA), (2c) two-nucleon emission followed by final-state interaction (FSI), (2d) three-nucleon emission with statistical distribution (3NA). Quasifree two-nucleon absorption is described by the reactions (2a) and (2b) where the third nucleon has only a small momentum and therefore can be regarded as a spectator. All three nucleons are involved in the reactions (2c) and (2d). Reaction (2d) is attributed to genuine three-nucleon absorption and has been observed with pions in flight [6,7,15–17] but not yet with pions at rest. Single-nucleon emission cannot be distinguished in principle from the *dn* final state (1) and the case (2c).

Experimentally, the branching ratios of isoscalar and isovector two-nucleon absorption can be determined from a coincidence measurement of back-to-back correlated *nn* and *pn* pairs. Both 2NA and FSI processes can be detected to a large extent with detectors set up at a relative angle of 180° by means of the registration of *pn*, *dn*, and *nn* coincidences.

This paper reports the results of a kinematically complete measurement using three different counter setups which cover almost the full phase space for the final state *pnn*. Two different parts of the phase space could be measured simultaneously by using detectors which are able to detect both neutrons and protons. Part of the data have been published already in a short version [11]. This paper is a full report giving more detailed results. A higher precision was obtained by reanalyzing the data with an improved neutron-detection efficiency code [18]. A large effort has been spent searching for evidence for a statistical three-nucleon emission process (2d).

Kinematics and experiment are described in Secs. II and III, respectively. In Sec. IV, the results from the three-body final state are shown in different representations like Dalitz plot and angular correlations. Relative branching ratios for the two-particle final state *dn* (1) and the three-particle channels (2a)–(2d) are given as obtained from the twofold and threefold coincidences. In Sec. V, the results are discussed with respect to the various concepts of pion absorption.

II. KINEMATICS

The nine degrees of freedom for the three-body final state *pnn* reduce to five due to energy and momentum conservation. For pion absorption at rest, particle emission is isotropic in space. Considering, e.g., the direction of the proton momentum (particle 1), we find two degrees of freedom corresponding to its spatial isotropy and one degree corresponding to a rotation of the three-legged event around this direction (Fig. 1). We are left with only two degrees of freedom and, therefore, two continuous variables are sufficient to describe the full dynamics. For example, the final state *pnn* is completely determined by the kinetic energies of the two detected particles or by one kinetic energy and one opening angle between two particles.

For both of the particles detected in coincidence, we have measured the two angles with respect to the beam axis and the kinetic energies. This corresponds to six measured quantities, where the four angles are used to determine the opening angle ϑ_{pn} or ϑ_{nn}, which is the only nontrivial angular information if no polarizations are measured. The remaining three variables are two kinetic energies and one opening angle, i.e., the events are kinematically onefold overdetermined. The resulting constraint in the data turned out to be very important since the background could be reduced significantly and the accuracy of the kinetic energies could be improved beyond the measured values by applying regression techniques.

It is quite suggestive to present data of the three-body final state in a Dalitz plot where each entry in the two-dimensional plot of the kinetic energies (e.g., T_p and T_{n_1}) contains the complete information about an event. A well-known property of the Dalitz plot representation is the constant phase-space factor. Hence, the measured two-dimensional density distribution of events is directly proportional to the moduli squared of the matrix elements, summed over the spin and isospin variables:

$$d^2W/dT_p dT_{n_1} = \text{const} \times \Sigma |M_{if}|^2\ . \tag{5}$$

The kinetic energies T have to be taken in the center-of-

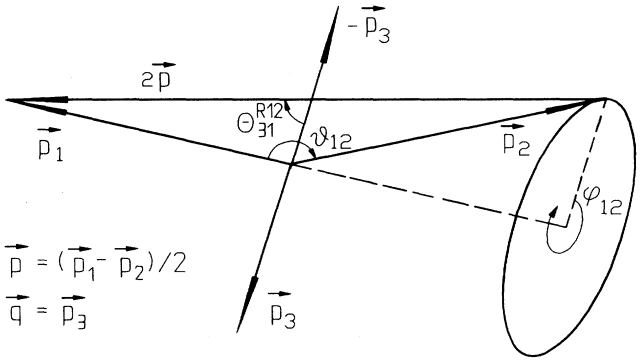

FIG. 1. Kinematics of the reaction $\pi^-_{\text{stop}}\,{}^3\text{He} \rightarrow pnn$. The indices (1,2,3) refer to any cyclic permutation of the particles (p, n_1, n_2). ϑ_{12} is the opening angle between the (measured) particles 1 and 2, p_3 the momentum of the (unobserved) recoil nucleon. Θ_{31}^{R12} is the center-of-mass emission angle of the recoiling particle 3 with respect to particle 1 in the rest frame of the particles 1 and 2.

mass system of the three final-state particles, which, for pion absorption at rest, is identical with the laboratory system.

Two types of Dalitz plot representations are used in this paper.

(i) In the first one, the kinetic energies of two particles are plotted in a Cartesian coordinate system and the energy of the third particle (T_{n_2}) is obtained from the distance to the tangent of $-45°$ (third axis). The boundary of the kinematically allowed region, which is approximately elliptical, is the two axes of the coordinate system and the tangent of $-45°$ [Fig. 2(a)].

(ii) In the second type, the three particles are treated in a completely symmetric way and the three energies are plotted along three directions oriented at 120° relative to each other. In this case, two new variables, the radius r, and the central angle Φ are used in a polar coordinate system with the center of the triangle as origin. Q denotes the total kinetic energy available in the final state pnn [Fig. 2(b)]:

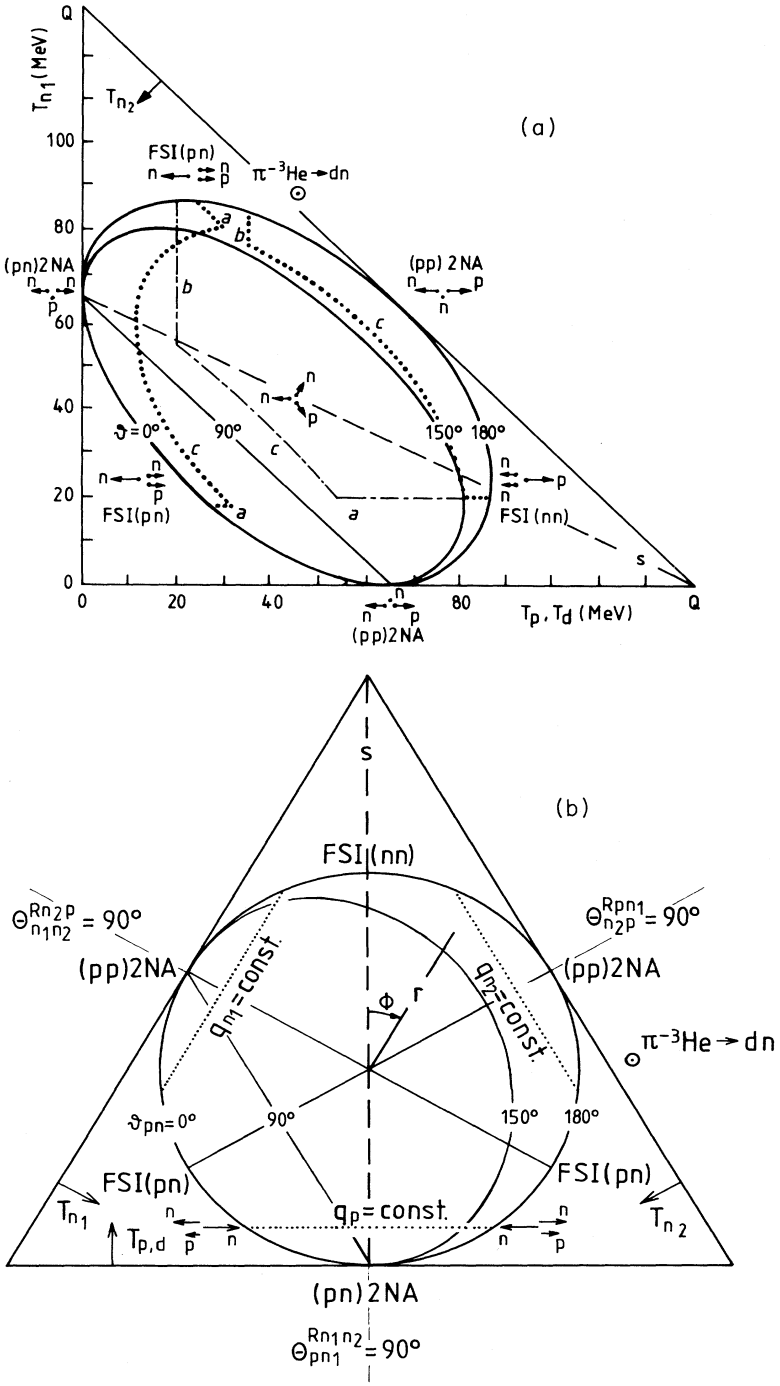

FIG. 2. (a) Dalitz plot of the reaction π^-_{stop} ^{3}He→ pnn in the rectangular representation. The momentum configuration of singular kinematical points on the perimeter (2NA,FSI) and center of the Dalitz plot are indicated by arrows. The dashed line is the symmetry line s. The kinematical point of the reaction π^-_{stop} ^{3}He→ dn is outside the allowed region of the three-particle final state pnn. The three areas indicated by the dashed-dotted and dotted-lines are the parts of the phase space covered by setups I and II (see Sec. III A). The (software) thresholds are indicated as a, neutron energies; b, proton energies; and c, angular acceptances. — · —, setup I, pn coincidences; ·····, setup II, nn (left) and pn coincidences (right). (b) Dalitz plot in the triangular representation. The height of the equilateral triangle is equal to the Q value of the reaction π^-_{stop} ^{3}He→ pnn. The "radius" r and azimuthal angle Φ are defined by Eqs. (6a) and (6b). Constant recoil momenta q are indicated by dotted lines.

$$r = \sqrt{3(T_{n_1} - T_{n_2})^2 + (3T_p - Q)^2}/Q \ , \tag{6a}$$

$$\cos\Phi = (3T_p - Q)/\sqrt{3(T_{n_1} - T_{n_2})^2 + (3T_p - Q)^2} \ , \tag{6b}$$

$$\begin{aligned} Q &= T_p + T_{n_1} + T_{n_2} \\ &= (m_{^3\mathrm{He}} + m_{\pi^-}) - (m_p + 2m_n) \ . \end{aligned} \tag{6c}$$

For equal masses and in the nonrelativistic limit, the boundary of the kinematically allowed region is a perfect circle. In our case, the deviation from a circle is only 1.1% at maximum. So, for a constant matrix element, i.e., for phase-space distributed particles in the final state, the projections of the density distribution are of very simple shape. For the projection onto the radius r, one obtains $dn/dr =$ const $\times r$, and $dn/d\Phi =$ const for projection onto the perimeter.

The boundary of the kinematically allowed region is the geometrical locus of all collinear events, i.e., of those events where the opening angles between any two of the three particles are 0° or 180°. Events with fixed opening angle ϑ between two particles are located on specific lines inside the allowed region. The point with $\vartheta = 120°$ between all three particles is located in the very center of the Dalitz plot. As there are two neutrons in the final state, the Dalitz plot is twofold symmetric around the symmetry line s, which is given by the condition $T_{n_1} = T_{n_2}$. Pairs of events which are symmetric to s contain identical physical information. Also shown in Fig. 2 is the kinematical point for the two-particle final state dn. Because of the larger Q value, it is outside of the kinematically allowed region of the pnn final state (Table I).

On the boundary of the physical region, there are six singular kinematical points which can be grouped into two families. The points labeled 2NA correspond to events where the energy of one nucleon is zero and the two others share the available energy in equal parts. The regions near the points (pp)2NA and (pn)2NA can be attributed to quasifree absorption on two protons and on a proton-neutron pair, respectively. The two absorbing nucleons are emitted back-to-back, while the third nucleon is a spectator. The label FSI corresponds to the kinematical condition, where one nucleon has the highest possible energy and the two others are emitted in opposite direction with vanishing relative velocity. Here, final-state interactions have to be expected between a proton and a neutron or between two neutrons [FSI(pn) or FSI(nn)]. The symmetry line s crosses the boundary in the points (pn)2NA and FSI(nn). The proton and neutron kinetic energies for the singular points 2NA and FSI are given in Table I.

TABLE I. Q values of the two- and three-particle final states and kinetic energies T of singular kinematical points [see (6c) and Fig. 2].

Channel		Q (MeV)	T (MeV)			
			p	d	n	n
π^-_{stop} ^{3}He $\rightarrow dn$		132.8		45.3	87.5	
π^-_{stop} ^{3}He $\rightarrow pnn$	(pn)2NA	130.6	0		65.3	65.3
	(pp)2NA		65.3		65.3	0
	FSI(pn)		22.2		86.2	22.2
	FSI(nn)		86.2		22.2	22.2

III. EXPERIMENT

A. Setup

The experiment was performed at the πE1 channel at PSI (formerly SIN). The momentum of the incoming beam was 220 MeV/c, which corresponds to a kinetic energy of 120 MeV for pions. The momentum spread was limited by slits to $\Delta p/p = 0.2$–$0.5\,\%$. The beam passed through two plastic scintillators (telescope counters T1 and T3) and a carbon degrader, which was surrounded by a conical copper collimator to eliminate the beam halo. Additional lead and paraffin shielding was used to suppress background originating from the region of the degrader. The last copper collimator and the telescope counter T3 (1 mm thick, 40 mm diameter, Fig. 3) reduced the background from the outer target container by 1 order of magnitude. Pions, muons, and electrons in the beam were separated by their time of flight (between the production target and the telescope counter T3) using the radio frequency (RF) of 50.7 MHz from the 590-MeV ring accelerator as time reference. An incoming pion was defined by the fast coincidence

$$\mathrm{T3}\pi = \mathrm{T1} \times (\mathrm{T3} \times \mathrm{RF}_\pi) \ , \tag{7}$$

where $(\mathrm{T3} \times \mathrm{RF}_\pi)$ is the coincidence between T3 and RF, selecting pions. The RF is also used as time zero for the time-of-flight information. An approximate adjustment of the degrader thickness was performed with the help of an additional veto counter T4 (20 cm × 20 cm), which was removed during data taking because of background reasons. The fine adjustment of the degrader was done by means of the dn coincidence rate.

The gaseous ^{3}He target was cooled by liquid ^{4}He to about 5 K. At this temperature, the density is enhanced by a factor of 60 as compared to normal conditions, but self-absorption of pionic x-rays and ionization losses of charged particles are still small. The ^{3}He target thickness was 130 mg/cm^2, whereas the total pion range (in carbon) was ≈ 40 g/cm^2. The (cylindrical) ^{3}He container of 12 cm length and 6 cm diameter consists of 100-μm-thick Mylar foil wrapped by 13 layers of superinsulation of 6 μm thickness each. The target container was surrounded by a cylindrical vacuum vessel with entrance and exit windows for the beam and side windows (of 175 μm of Mylar each) for the charged particles and the x-rays.

The reaction products were detected in a charged-particle detector S and two identical time-of-flight counters N1 and N2. The counters N1 and N2 were used to detect both neutrons and charged particles. The detectors were arranged in different ways for the various measuring periods. Setup I used S, N1, and N2 (Fig. 3,

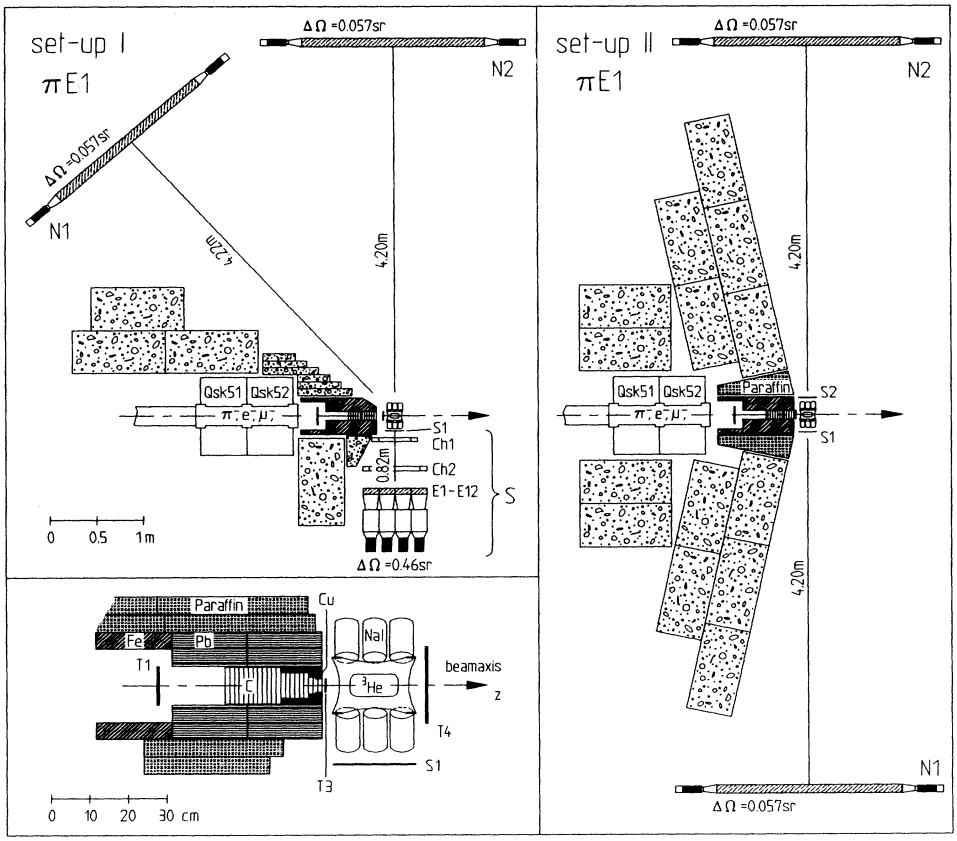

FIG. 3. Setups I and II (see text). The inset (bottom left) shows details of the degrader and the ^{3}He kryotarget. The conical form of the carbon degrader together with the various shielding materials suppresses background from the halo of the degraded beam. The veto counter T4 was removed after the adjustment of the range curve. The NAI (Tl) detectors were mounted beneath the ^{3}He target close to the Mylar windows of the target vessel. Distances and solid angles of detectors S, N1, and N2 are given with respect to the front of the plastic scintillator arrays. For setup III, the distances between the center of the target and the counters N1 and N2 were 3.0 m each resulting in a solid angle of $\Delta\Omega = 0.107$ sr.

left: *pn* and *dn* coincidences), setups II (Fig. 3, right) and III used N1 and N2 (*pn*, *dn*, and *nn* coincidences detected simultaneously). The phase space covered for the final state *pnn* is indicated in Fig. 2(a).

For all measurements, a coincidence between two detectors was required. Figure 4 shows the geometrical acceptance for the detection of particle pairs as a function of the opening angle ϑ. The finite size of the target has been taken into account. The charged-particle detector S had a proton detection threshold of $\approx$ 18-MeV kinetic energy. Hence, the part of the *pnn* phase space with proton energies larger than 18 MeV was measured in setup I. Proton energies below the threshold energy were accessible via the *nn* coincidences in setups II and III. In all setups, the *dn* final state has been used as monitor. The data were registered event-by-event via CAMAC and recorded on magnetic tape using a PDP 11/40.

B. Charged-particle detector S

The totally absorbing counter hodoscope consists of a 4×3 matrix of optically isolated plastic scintillators E1–E12 of NE102A (17 cm × 17 cm × 8 cm each) connected by Lucite light guides to 11 cm photomultiplier tubes (Philips XP 2241). The depth of 8 cm is sufficient to stop 100-MeV protons. For tracking, two multiwire proportional chambers (MWPC) CH1 and CH2 were used with a wire spacing of 2 mm. The pulse height from a 1-mm-thick plastic scintillator S1 discriminates protons and heavier particles from scattered electrons emerging from the target region. A proton or heavier charged particle is defined by the fast coincidence

$$S_c = T3\pi \times S1 \times \sum_{i=1}^{12} E_i \,, \tag{8}$$

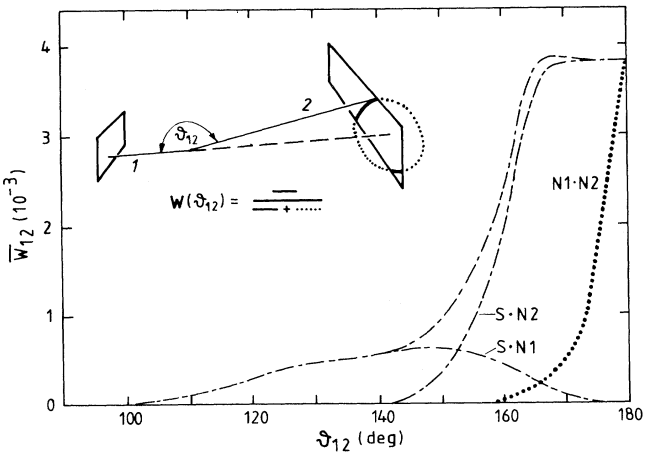

FIG. 4. Angular acceptances of setup I (—·—) and setup II (·····) as a function of the opening angle ϑ_{12} between the two coincident particles. The detector combinations S×N1 and S×N2 of setup I are shown separately. The total acceptance for one opening angle is the sum over all possible impact points of trajectory 1.

which in turn triggers the CAMAC readout cycle of the MWPC's. The track information from the MWPC's has been used only in the off-line analysis.

Energy and time resolution of the E counters were determined by exposing them to a 220-MeV/c pion beam. Traversing the 17-cm-wide plastic material, the pions deposited an energy of 50 MeV. The resolutions were found to be $\Delta E/E = 4\%$ (FWHM) and $\Delta t = 300$–400 ps (FWHM), corrected for the time uncertainty of the accelerator RF [$\Delta t_{RF} \leq 500$ ps (FWHM)]. The gain of the photomultipliers was monitored during the data taking by light emission diodes (LED's) which were inserted into the light guides. After each cycle of 1000 physical events, 64 test events were recorded. The light output was varied sequentially by attenuating the pulser voltage by 0, 4, 8, and 12 dB. The pulse heights of the LED's were calibrated in a separate measurement with minimum-ionizing cosmic-ray muons. From the muon signal, the light output for protons and deuterons was calculated and an absolute energy calibration achieved [19–22]. An independent calibration point was obtained with monoenergetic deuterons of the dn channel, which arrive at the E counters with an energy of ≈ 36 MeV. The energy at the target vertex is obtained after correction for energy loss using the track information of the MWPC's. Due to the 180° correlation, the check of the energy calibration with the deuterons could be performed only for the two central counters E6 and E7. The accuracy for reconstructing the deuteron energies from the pulse heights is demonstrated in Fig. 5.

Particle identification, performed by the combination of time of flight and kinetic energy as derived from the pulse heights, is shown in Fig. 6 for the central counter E6 and the peripheral counter E12. Due to the extended size of the ^{3}He target, a few deuterons from the dn final state are also detected by E12. No accumulation of monoenergetic deuterons is seen in the corresponding empty target measurement.

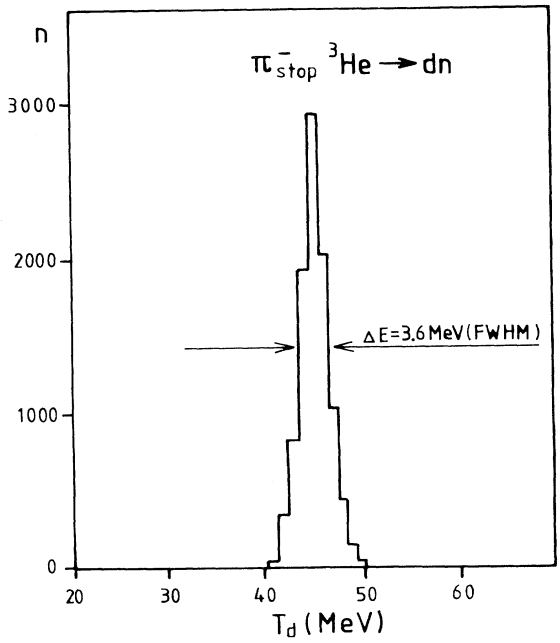

FIG. 5. Energy spectrum of the monoenergetic deuterons from the reaction π^-_{stop} ^{3}He→ dn after correction for energy loss and flight path (setup I).

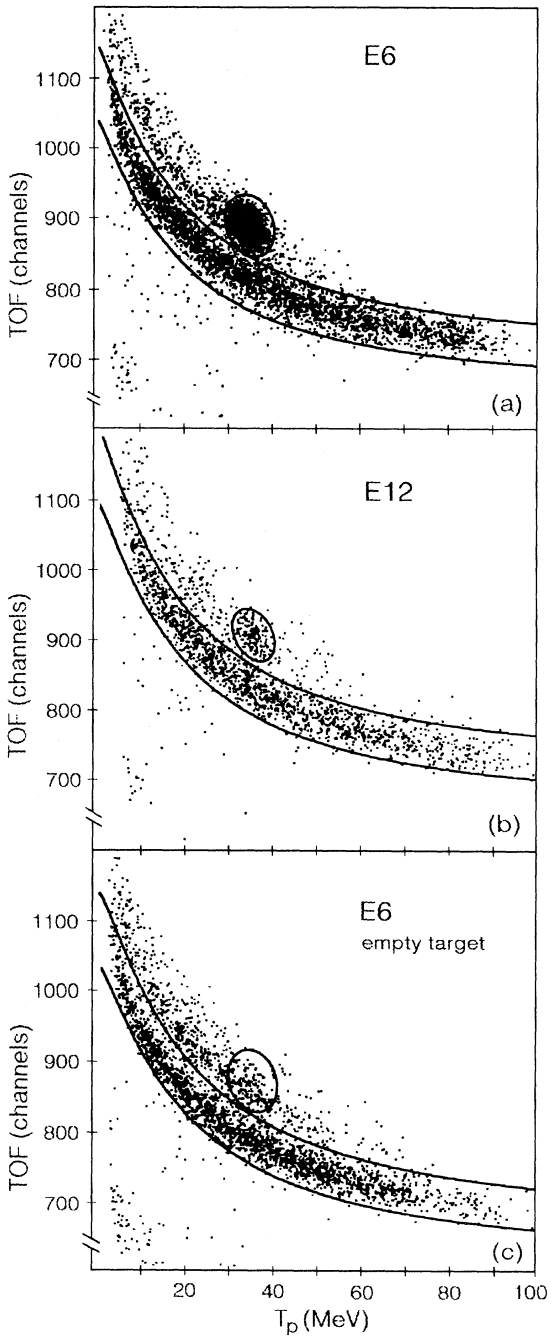

FIG. 6. Particle separation by time of flight and kinetic energy as measured with the individual counters E6 and E12 of the charged-particle detector S. The two hyperbolas define the window for the accepted protons, the ellipse the window for the (monoenergetic) deuterons: (a) central counter (E6); (b) peripheral counter (E12); (c) central counter (E6), empty target measurement.

Figure 7 shows the projections of the target-vertex distribution on the y-z plane for pn [Fig. 7(a)] and dn [Fig. 7(b)] coincidences. For pn coincidences, background events are seen from reactions in the telescope counter T3 and the Mylar entrance window of the target vessel surrounding the fiducial ^{3}He volume, whereas dn coincidences are observed only from the ^{3}He volume. The uniformity of the detector response was checked with the distribution of the reconstructed impact points over the areas of the E counters. The efficiency reduction for protons and deuterons due to nuclear reactions of the particles has been estimated from the data given by Measday *et al.* [23]. The corrections are 5% at maximum for energies of 80 MeV and decrease to 0.5% for 20-MeV protons.

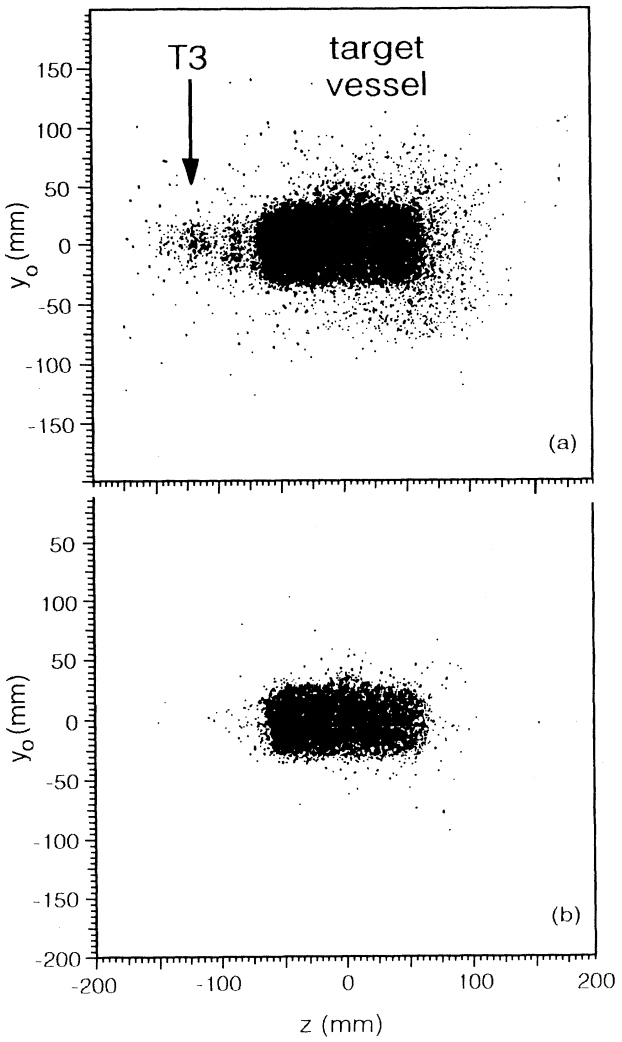

FIG. 7. Reconstruction of the target vertex using the track information obtained from the MWPC's. (a) All charged particles: The accumulation between the telescope counter T3 and the target vessel is due to reactions in the entrance window of the target vacuum container. (b) Back-to-back correlated deuteron-neutron coincidence required.

C. Time-of-flight counters N1 and N2

Each of the two position-sensitive time-of-flight counters N1 and N2 consists of four identical modules. Their main components have been used previously in (π^-, nn) experiments [24]. Each module, built up of 12 optically isolated plastic scintillator rods of NE 110 (200 cm $\times$6 cm$\times$1.5 cm) is forming a matrix of 12 cm $\times$9 cm with two layers in height and six layers in depth. The module is viewed on either side by one 5 cm photomultiplier tube (56 DVP) connected to all 12 rods with one Lucite common light guide covering half of the end surface of all the rods. Six 1.4 cm photomultiplier tubes (SEN 1045) are attached directly to the scintillator rods with three tubes above and three tubes below the light guide where one tube overlaps with two rods (except the tube attached to the first or to the sixth rod). By displacing the 1.4 cm tubes by one rod at opposite sides of a module, the hit pattern is obtained unambiguously. The total sensitive volume of each counter is 200 cm $\times$ 48 cm $\times$ 9 cm. Pulse height and timing information are obtained from the 5 cm tubes. With the hit pattern as obtained from the 1.4 cm tubes, the tracks of recoiling protons can be reconstructed and multiple hits can be identified. Each counter forms a 8 $\times$ 6 matrix in height and depth. The first of the six layers is used as veto detector to separate neutrons from charged particles. An event is accepted by a fast logic circuit, whenever coincident signals from either side of a module occur together with a valid trigger from the charged-particle detector S (setup I) or from the second time-of-flight counter (setups II and III) within a time window of 200 ns.

Particle separation is obtained by combined time-of-flight and pulse-height information. In Fig. 8(a), pulse height vs time of flight is displayed for events triggering the first layer of N2 in setup I. Because the trigger condition requires a charged particle in the detector S, only a few protons are detected as accidentals in the first layer of N2. Beneath the proton hyperbola is the continuum of neutron induced events. The horizontal band (around channel 700) is due to the monoenergetic neutrons from the dn channel. Quantitatively, the background from neutron-induced reactions triggering layer 1 is determined by applying the charged-particle cuts from layer 1 to layer 2 requiring layer 1 in anticoincidence (the reduction in neutron flux can be neglected).

The entries in Fig. 8(b) are due to neutral particles only, because a trigger is required from any layer 2–6 in anticoincidence with layer 1. Again, the monoenergetic neutrons of the dn channel are clearly visible. The distribution of these neutrons is used for the time-of-flight calibration. The increase of the time of flight at small pulse height is due to time walk at the discriminator threshold.

In setup II, the time-of-flight counters are used also as charged-particle detectors. Figure 8(c) shows the well-separated proton and deuteron distributions from N1 triggered by the first layer. The concentration of entries in the upper window belongs to the monoenergetic deuterons arriving at the counter with a kinetic energy of about 29 MeV. The coincidence with the scintillation

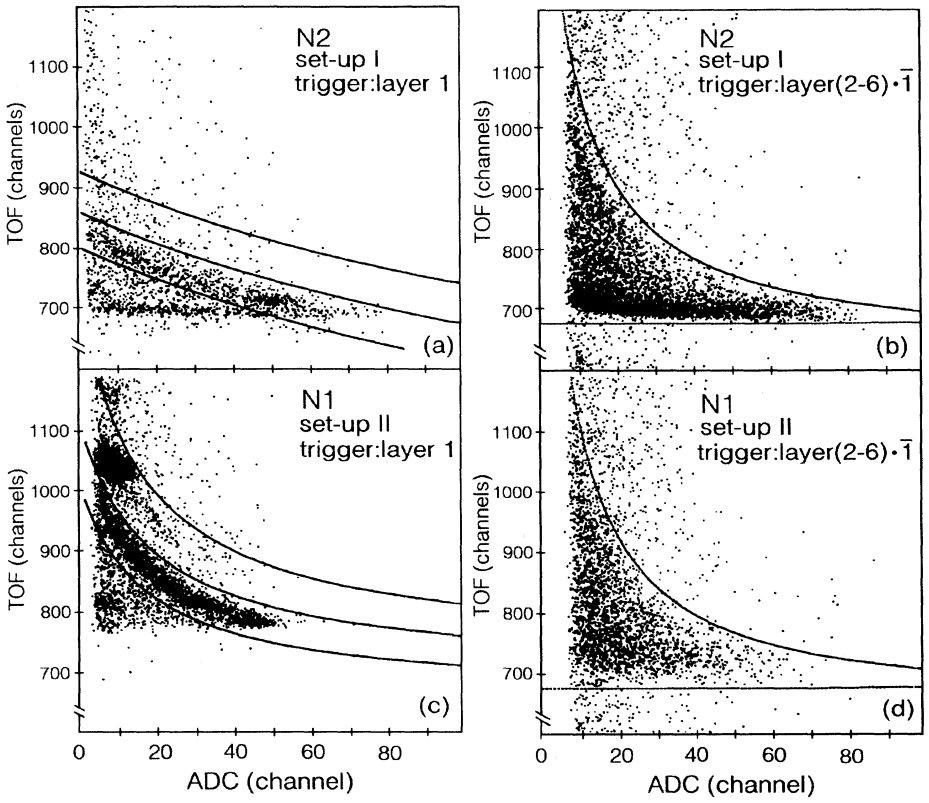

FIG. 8. Particle separation with time of flight and pulse height with the counter N1 and N2. (a) "Charged particles," N2 triggered with first layer (setup I): The band from the monoenergetic neutrons [see also Fig. 8(b)], which convert in the first layer, crosses the proton hyperbola at larger pulse heights (ADC ch. ≈ 50); (b) "neutral particles," N2 triggered with layers 2–6 in anticoincidence with layer 1 (setup I); (c) "charged particles," N1 triggered with first layer (setup II); (d) "neutral particles," N1 triggered with layers 2–6 in anticoincidence with layer 1 (setup II).

counters S1 for N1 (or S2 for N2) (Fig. 3), required for charged particles in the off-line analysis only, reduces the background substantially.

Setup II is asymmetric in the sense, that the outer target vessel contains a thin Mylar window in the direction towards N1, but a 2-mm-thick steel wall towards N2. This wall is pervious to neutrons but not to the deuterons. So, requiring the coincidence (N1 × N2), no monoenergetic neutrons from the *dn* channel could be registered by N1 [Fig. 8(d)].

The impact point of the particles along the horizontal direction of the rods is determined from the left-right time difference of the signals of the 5 cm phototubes. The calibration for the distribution of impact points along the rod is obtained from the *dn* coincidences. The deuteron trajectories were measured with the MWPC's (in setup I) allowing the calibration of the time encoders and the determination of the light-propagation velocity in the rods. The position resolution in the direction of the rods is given by the time resolution of the photomultiplier pulses and the intrinsic resolution of the plastic bar. A resolution of ±9 cm (FWHM) has been obtained for setup I. In the vertical direction, the uncertainty is 6 cm as given by the height of one scintillator rod. The coordinate in the particle's flight direction is determined by the first layer fired as derived from the pattern of the small tubes with an uncertainty corresponding to the rod thickness of 1.5 cm.

The position resolutions of the neutron counters essentially determine the angular resolution of the opening angle ϑ in setup I. The position resolution at the charged particle detector is ≈ 2 mm corresponding to the wire spacing of the MWPC's and hence its angular resolution is an order of magnitude better. For setup I, the deviation of $\Delta\vartheta = 1.1°$ from the ideal value of 180° for the angular correlation of the two-particle final state reflects the finite position resolution of N2. In setups II and III, no MWPC's were used, i.e., the angular resolution is given by folding the resolutions of N1 and N2 yielding $\Delta\vartheta = 1.7°$.

The time differences for slowing down and stopping the pions in the ^{3}He gas are up to 3 ns over the target length of 12 cm. Hence, a vertex-dependent time-of-flight correction was applied in addition to the correction from the individual flight path of each particle. Also, time-walk corrections are indispensable.

The time of flight thus achieved in setup I for the monoenergetic neutrons from the *dn* channel was 34.2±1.1 ns which corresponds to a kinetic energy of 86.9 ± 6.4 MeV (34.5 ± 2.0 ns or 88.0 ± 10.5 MeV in setup II). The energy spectrum obtained for setup I is shown in Fig. 9. For charged particles, the measured time of flight was corrected according to the energy loss along the flight path. The deuteron time of flight was determined to be 74.3 ± 2.8 ns in setup I corresponding to a kinetic energy of 45.4 ± 2.6 MeV. A detailed description of the corrections applied is given elsewhere [21].

The neutron-detection efficiency ε_n is a function of the discriminator threshold and the neutron energy. In order to obtain a homogeneous efficiency over the full length of

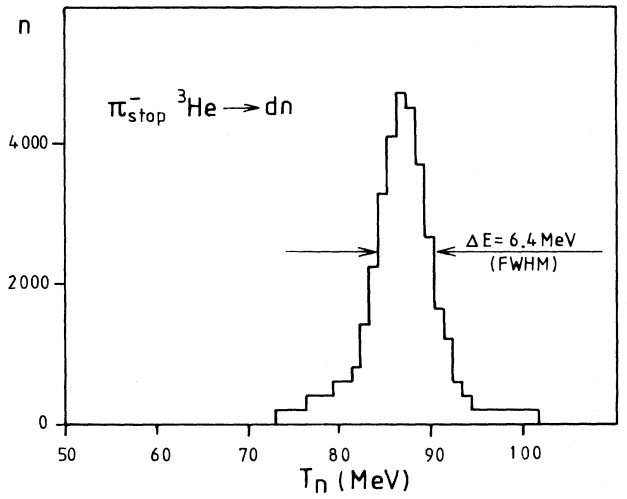

FIG. 9. Energy spectrum of the monoenergetic neutrons from the reaction π^-_{stop} ^{3}He→ dn reconstructed from time-of-flight measurements to be 86.9 ± 6.4 MeV.

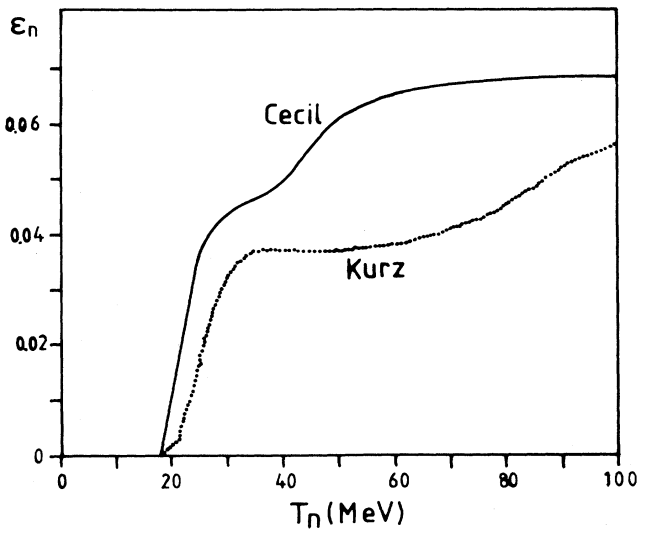

FIG. 10. Neutron-detection efficiency ε_n of layers 2–6 of the neutron counter N1 or N2 as calculated with the CECIL code [18] (solid curve) for a threshold of 12-MeV electron-equivalent energy (= 20-MeV proton-equivalent energy). For comparison, the results obtained from Kurz' code [25] are given for the same threshold (dotted curve).

the detector modules, a software threshold was applied to the geometric mean $\sqrt{P_L P_R}$ of the pulse heights P_L and P_R from the large photomultipliers on the left and right sides of each module. Since the hardware coincidence required signals from either side, the software threshold was set slightly above the corresponding hardware thresholds of P_L and P_R. In order to avoid edge effects due to deviations from exponential light attenuation at the very ends of the rods a software cut was applied to the left-minus-right arrival time, which corresponds to a cut on the extreme 10 cm on each side. The absolute energy calibration of the pulse heights was obtained with an accuracy of 1–2 MeV from the pn coincidences itself with the time of flight of the protons corrected for energy loss.

Because of its strong energy dependence, the precise knowledge of the neutron-detection efficiency is very important. In our first data analysis [11], the efficiency code of Kurz [25] had been used, which had been reported to be reliable and to agree well with experimental data at that time [26]. Later, the CECIL code [18] became available, a Monte Carlo code which uses more recent input data, especially for the inelastic neutron-carbon reactions. Recent measurements on neutron efficiencies demonstrate the superior quality of the CECIL code [27]. Therefore, all results presented in this paper are obtained using the CECIL code. The software threshold was set to 12-MeV electron-equivalent energy which corresponds to 20-MeV proton energy. The difference between the Kurz code and the CECIL code turns out to be significant (Fig. 10). In the 2NA regions, i.e., at $T_n \approx 60$ MeV, the difference is $\approx 30\%$. Consequently, our new results differ to some extent from the earlier publications [11,28].

D. Detection of pionic K x rays

A large solid angle and good background suppression were necessary for the detection of the pionic K series (transitions to the $1s$ state) having energies of 10.7–14 keV. With 6 NaI detectors of 0.1 mm thickness and 4.54 cm active diameter, each one mounted 12 cm below the target (Fig. 3), a solid angle of 0.4 sr was covered. The energy resolution was 35% (FWHM) and the intrinsic detection efficiency was close to 100% at 11 keV [29]. The energy calibration and efficiency of the detectors was monitored with ^{57}Co (6.4 keV) and ^{109}Cd (22 keV) radio-active sources of known activity. Figure 11 shows the x-ray spectrum taken in coincidence with nn, pn,

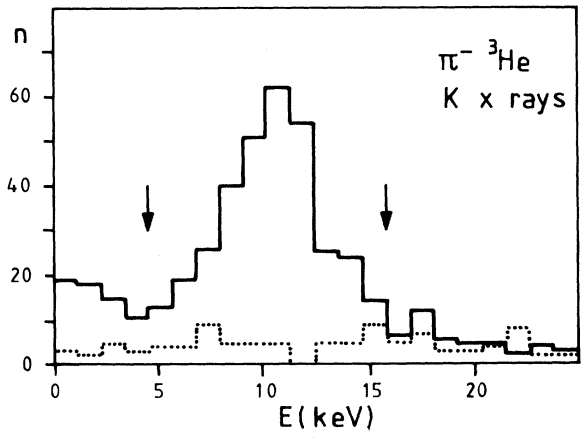

FIG. 11. Energy spectrum of x rays as measured with the NaI(Tl) detectors in coincidence with proton-neutron, deuteron-neutron, and neutron-neutron coincidences detected with setup II (solid line, ^{3}He measurement; dotted line, empty target measurement, normalized to the number of incoming pions of the ^{3}He measurement). The arrows indicate the cut applied to the energy range to select the pionic K series from ^{3}He.

and *dn* coincidences. A cut on the energy region of the pionic ^{3}He K x-rays was applied for the analysis of the threefold coincidences for both ^{3}He and the background measurements.

E. Data acquisition

The experiment was controlled on line by a specially tailored program system running on a PDP 11/40 [30]. Besides the data readout via CAMAC, the system handles communication, histogramming, and data storage on magnetic tape. The length of an event vector was typically 200-300 16-bit words containing an event identification, time-of-flight, and pulse-height information, the pattern of the attached scintillators, the MWPC information, and scaler contents. The system automatically switched between physical events (1000 events) and test triggers generated by the LED's (64 test events).

The readout cycle started whenever a coincidence between two detector arms was accepted by the hardware logic $[S_c \times (\mathrm{N1} + \mathrm{N2})]$ for setup I or (N1 $\times$N2) for setups II and III. At the typical event rate of 40/s, the dead time of the recording system was negligible. The details of the trigger logic are described elsewhere [21,22].

F. Data analysis

Due to the very small target thickness as compared to the width of the Bragg peak, only a small fraction of the beam could be stopped in the ^{3}He gas. From the rate of incoming pions T3π (7) and the *dn* coincidence rate, the fraction of pions stopping in the ^{3}He gas was determined to be 1–2 %. Therefore, background subtraction was performed by subtracting the events from empty target measurements which were normalized to the number of incoming pions. For each setup, a background measurement has been carried out with a statistics comparable to the ^{3}He measurement.

The data analysis was performed in steps. In a first step, the set of on-line information including the MWPC data was checked for completeness. In a second step, the kinetic energies at the vertex were reconstructed from pulse heights and time information including corrections for energy loss of the charged particles. The opening angle between the two coincident particles was determined.

The third step contains several stages. The events were weighted according to detection efficiency and geometrical acceptance. An efficient background suppression results from the fact that the final state *pnn* is onefold kinematically overdetermined. Only events up to a 3σ deviation (σ^2 is the variance of the resolution function) from the maximum of the likelihood function were accepted, which reduces the background by $\approx$ 75% for *pn* and by $\approx$ 50% for *nn* coincidences. The background mainly originates from pion absorption in nuclei of the target container (carbon and oxygen). For quasifree absorption on NN pairs, kinetic energies around 60 MeV are preferred not only for ^{3}He but also for carbon and oxygen. After applying the kinematical constraint, the fraction of background events left is $\approx$ 30% for *pn* and *nn* coincidences for the setups II and III. For setup I, the trigger is much cleaner due to the track reconstruction and the shorter flight path and therefore, the fraction of background events left is $\approx$ 10% only. The two-body final state *dn*, threefold kinematically overdetermined, is already very clean due to its collinear signature and its fixed energy. In this case, the reduction caused by the kinematical constraint is only 2% for the full target measurement, but 95% for the empty target measurement. Furthermore, the kinematical constraint provides improved values for the measured kinetic energies of the *pnn* final state. For the opening angle ϑ it turned out, that within its resolution ($\Delta\vartheta = 1.1°$) the variations of the kinetic energies are small compared to their accuracy. Therefore, the opening angle has been taken to be exact in the constraint calculation.

In a last step, the spectra from the empty target measurements, normalized to the number of incoming pions, are subtracted from the corresponding spectra of ^{3}He measurements. In Table II, the numbers of events having passed the complete analysis are listed for both the ^{3}He and the empty target measurements.

TABLE II. Total statistics accumulated in the measuring periods I, II, and III. The total number of incoming pions accepted by the telescope counter T3 is used for normalization. The numbers for deuteron-neutron, proton-neutron, and neutron-neutron coincidences passing the cuts of the analysis are given without (*dn*, *pn*, *nn*) and with coincident x-rays detected in the NaI detectors ($dn \cdot x$, $pn \cdot x$, $nn \cdot x$). The kinematical constraint is applied for 3σ of the energy-resolution function (see text).

	Setup I		Setup II		Setup III	
	^{3}He	Background	^{3}He	Background	^{3}He	Background
T3π	410×10^9	136×10^9	245×10^9	147×10^9	625×10^9	737×10^9
dn	100 840	41	33 899	82	27 000	
pn	94 005	3 404	8 109	1 575	9 000	1 320
nn			7 709	2 337	10 200	2 995
$dn \cdot x$	268	0	202	1	213	0
$pn \cdot x$	236	12	38	5	86	7
$nn \cdot x$			35	9	126	6

IV. RESULTS

A. Dalitz plot of the *pnn* final state

The density distributions in the Dalitz plot, as obtained from the measured kinetic energies, are shown in Fig. 12. A software cut restricts the protons to energies above 20 MeV (setup I) and 35 MeV (setup II), respectively. In Fig. 12(a), for $T_p > 20$ MeV and in Fig. 12(b) for $T_p > 35$ MeV, the events above the symmetry line s are from the measured proton-neutron coincidences, where neutron 1 has the high energy and neutron 2 has the low energy ($T_{n_1} > T_{n_2}$). Below the line s, neutrons 1 and 2 have exchanged their roles. The energy of neutron 2 is calculated using the relation $T_{n_2} = Q - T_p - T_{n_1}$. Proton-neutron coincidences with neutron energies below the symmetry line s are rejected in the analysis in order to avoid double counting. Branching ratios are determined from the events with $T_{n_1} > T_{n_2}$ only. All events displayed in Fig. 12(b) with $T_p < 15$ MeV are from measured neutron-neutron coincidences. For the calculation of branching ratios, the *nn* count rate is divided by 2 before relating it to the *pn* count rate.

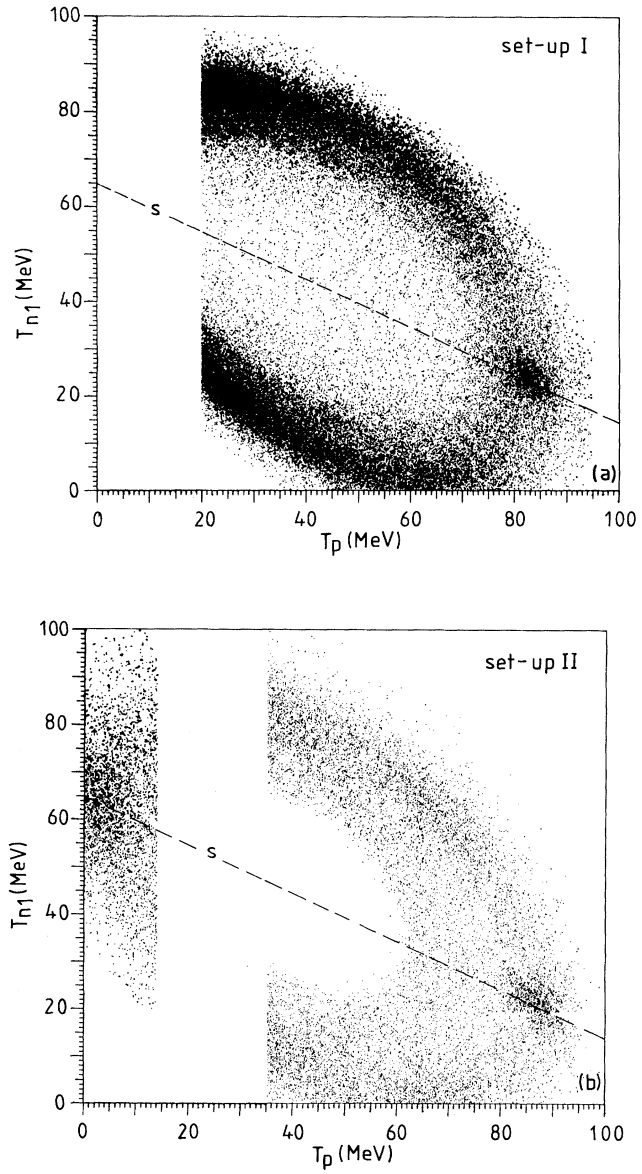

FIG. 12. (a) Two-dimensional density distribution from proton-neutron coincidences as measured with setup I. (b) Two-dimensional density distribution from neutron-neutron (left) and proton-neutron coincidences (right) as measured with setup II. The proton-neutron coincidences below the symmetry line were obtained using the twofold symmetry of the Dalitz plot (see text). All energy thresholds are due to software cuts. The points represent the directly measured energies. No corrections for efficiency and acceptance are applied.

The results from setups I and II are presented together in a contour plot (Fig. 13), which is constructed from the improved values of the kinetic energies as obtained from the constraint calculation (see Sec. III F). Only a very small part of the (*pn*)2NA phase space was not covered. The missing intensity from this region was inferred from the (*pp*)2NA region (totally covered with setup I), assuming similar shapes for both 2NA regions.

The interior of the Dalitz plot is depleted, i.e, collinear events are preferred in the three-particle final state *pnn*. Two classes of highly populated regions show up: (i) quasifree absorption on NN pairs of the ^{3}He nucleus (*pn*)2NA and (*pp*)2NA, where absorption on a proton-neutron pair is the dominant mode, (ii) final-state interaction FSI(*pn*) and FSI(*nn*) of two nucleons emitted with small relative momentum, whereas the third nucleon is

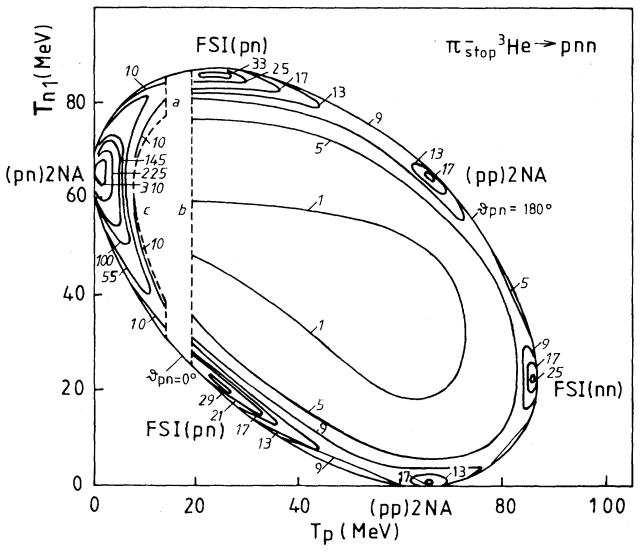

FIG. 13. Contour Dalitz plot of the reaction π^-_{stop} ^{3}He→ *pnn* combining the data from setups I and II. The "improved" kinetic energies as obtained from the constraint calculation are used. The distributions are corrected for efficiency and acceptance. The numbers at the contour lines reflect the actual intensities (in a.u.). *a*, off-line energy threshold for setup II; *b*, off-line energy threshold for setup I; *c*, off-line threshold of acceptance for setup II.

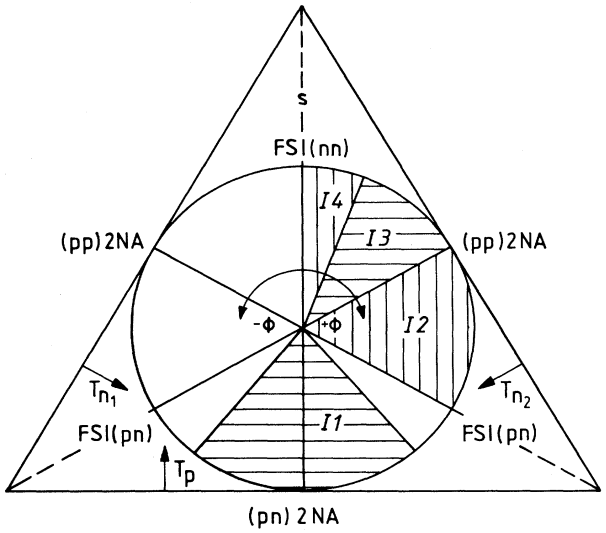

FIG. 14. Cuts defining the regions I1–I4 using the triangular Dalitz plot (see Table III).

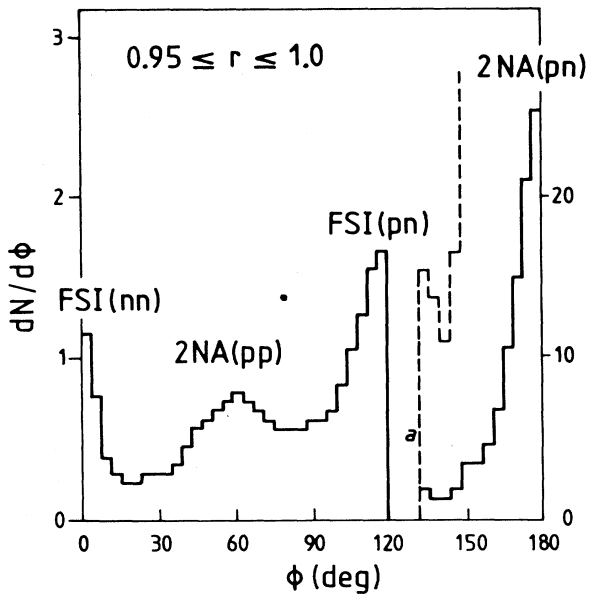

FIG. 15. Φ distribution near the boundary of the kinematically allowed region. Note the change of the scale at Φ = 120°. *a*: software threshold of acceptance in setup II.

emitted in the opposite direction with nearly the maximum possible momentum.

The angle Φ (see Sec. II) is used for a quantitative determination of the strengths of the 2NA and FSI regions in a model-independent way. The separation is performed by cutting along radii r i.e., along lines with Φ =const. Four regions I1–I4 are defined, which are related to the physical regions 2NA and FSI (Fig. 14). The physical regions are approximated by the relations given in Table III and the symbols 2NA and FSI have to be understood in this sense in the following quantitative discussion. A comparison with theoretical calculations is unique applying the same cuts I1–I4 to define the relative yields.

In order to show the density variations for the 2NA and FSI channels (2a)–(2c), the two-dimensional density distribution is projected on the kinematic boundary of the (triangular) Dalitz plot. By using equidistant intervals of the central angle Φ, each bin of the Φ distribution corresponds to a sector of equal area in the Dalitz plot. The Φ distribution (for $0.95 \leq r \leq 1$) is shown in Fig. 15.

The second column of Table IV shows the yields of the 2NA and FSI regions normalized to the *dn* final state, which is the direct result of this experiment. Truöl *et al.* have measured the branching ratios of the charge exchange (3) and radiative capture reaction (4) [12]. The branching ratio of 0.682 for the sum of the two absorption channels *pnn* (1) and *dn* (2) is then just the complement and has been used here to calculate the intensities per pion stop (third column of Table IV).

B. 2NA regions

Kinematically, the momentum distribution of the recoil nucleus (i.e., a proton or a neutron in the case of ^{3}He) is equal to the momentum distribution of the absorbing NN pair. The momentum distribution of the neutron, recoiling against the absorbing proton-proton pair, is shown in Fig. 16. The best fit to a 1*s* harmonic-oscillator wave function given by $(1/p)dN/dq \sim q^2\exp(-q/q_0)^2$ is obtained with $q_0 = 96 \pm 3$ MeV/c (1σ). The enhancement at $q \approx 230$ MeV/c stems from tails of the FSI region. The spectrum is compared to the proton momentum distribution obtained from quasifree electron scattering [31,32]. The overall agreement is quite good despite the fact that the spectrum is shifted to smaller momenta by ≈ 10 MeV/c in the case of electron scattering. A similar agreement was found already for pion absorption in flight [33]. The momentum distribution of neutrons in ^{3}He has been

TABLE III. Cut definition of regions in the Dalitz plot for a quantitative determination of the 2NA and FSI transition strengths (see Fig. 14). $\Phi_{central}$ refers to the angle of the center line of the individual region.

Cut	Definition of cut	Region	$\Phi_{central}$ (deg)
I1	$-140° \leq \Phi < -180°$ and $140° \leq \Phi \leq 180°$	(*pn*)2NA≡ 0.5·I1	180
I2	$60° \leq \Phi < 120°$	FSI(*pn*)≡ 2·(I2−I3)	120
I3	$21° \leq \Phi < 60°$	(*pp*)2NA ≡ 2·I3	60
I4	$0° \leq \Phi < 21°$	FSI(*nn*) ≡I4	0

TABLE IV. Measured branching ratios of the 2NA and FSI regions as defined in Table III for the final state *pnn* normalized to the two-particle final state *dn*. In order to obtain the yield per stopped pion, the sum of the branching ratios for the *pnn* and *dn* final states is normalized to 0.682 [12]. In the last column the K yields are given (branching ratio of absorption from the atomic 1*s* state to absorption from all atomic states). The K yield for the *dn* final state is calculated from the results of the measurements described in [28,29].

	Yield/($\pi^-_{\rm stop}$ ^{3}He$\rightarrow$ *dn*)		Yield/$\pi^-_{\rm stop}$		Y_K
	a	b	a	b	
(*pn*)2NA	$2.78 \pm 0.39 \pm 0.20$		$0.362 \pm 0.051 \pm 0.026$		0.29 ± 0.09
FSI(*pn*)	$0.87 \pm 0.07 \pm 0.06$		$0.113 \pm 0.009 \pm 0.008$		0.33 ± 0.08
(*pp*)2NA	$0.44 \pm 0.04 \pm 0.03$		$0.057 \pm 0.005 \pm 0.003$		0.28 ± 0.09
FSI(*nn*)	$0.15 \pm 0.03 \pm 0.01$		$0.020 \pm 0.004 \pm 0.001$		0.22 ± 0.09
π^- ^{3}He$\rightarrow$ *pnn*	4.24 ± 0.62[c]		0.552 ± 0.065[c]		0.30 ± 0.06
π^- ^{3}He$\rightarrow$ *dn*	1.0		0.130 ± 0.015[c]		0.47 ± 0.04

[a]Total error from the analysis of one measurement.
[b]Systematic error from combining different setups.
[c]The error from the separation of regions in the Dalitz plot has not been considered here.

measured by quasielastic proton scattering [34], where, however, a much broader q distribution has been found. In a representation equivalent to Fig. 16, the maximum is at $\approx$ 180 MeV/c thus q_0 being a factor of 2 larger than in this experiment. The discrepancy between the proton and the electron induced experiments might be due to strong initial- and final-state interactions.

As can be seen from Fig. 17(a), the opening-angle distributions of the (*pn*)2NA and (*pp*)2NA regions are of similar shape, i.e., the momentum distributions of absorbing *pn* and *pp* pairs are the same in ^{3}He within the

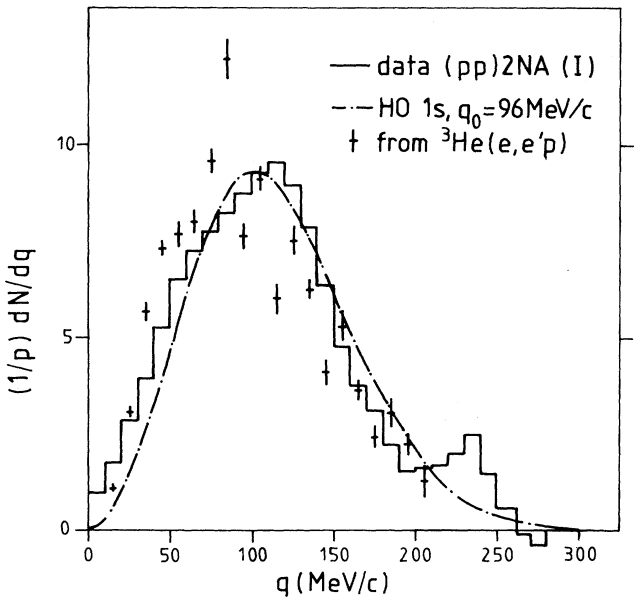

FIG. 16. Recoil-momentum distribution of the spectator neutron in the (*pp*)2NA region (setup I). —·— , 1*s* harmonic-oscillator wave function with q_0 = 96 MeV/c; +, momentum distribution of protons measured by use of the reaction ^{3}He$(e,e'p)$ [31]. The distributions are normalized to equal areas. The fit to q_0 was obtained with the data for $0 \le q < 210$ MeV/c.

experimental errors. In Fig. 17(b), the difference in the angular distributions is demonstrated for correlated and statistical emission (Monte Carlo simulation) of nucleon-nucleon pairs.

According to the definition of quasifree absorption at rest, no angular-momentum transfer is expected from the absorbing nucleon pair N_1N_2 to the spectator nucleon N_3, which in the case of ^{3}He is (mostly) in a relative s state to the absorbing pair. An s state corresponds to an isotropic distribution of the angle Θ_{31}^{R12} of the spectator recoil momentum $\vec{q} = \vec{p}_3$ relative to the momentum $\vec{p} = \frac{1}{2}(\vec{p}_1 - \vec{p}_2)$ of the nucleon pair N_1N_2 [35,36] (see Fig. 1). Because the cut I3 (see Fig. 14) does not preserve this isotropy, the measured distribution of Θ_{31}^{R12} is compared with the respective Monte Carlo generated spectrum for (*pp*)2NA absorption (Fig. 18). A small deviation is observed, which might be attributed to FSI.

C. FSI regions and two-particle final state *dn*

The nucleon-nucleon interaction at small relative momenta leads to an angular correlation (Fig. 19) which is narrower than in the 2NA regions. In the FSI(*pn*) region, both $^1S_0$ and $^3S_1$ *pn* interactions are possible, whereas the two neutrons in the FSI(*nn*) region are restricted to a $^1S_0$ partial wave (in the limit of low relative momenta). The steep decrease of the r distribution for FSI(*pn*) suggests that the $^1S_0$ partial wave is the dominant contribution (Fig. 20). The result of a numerical analysis, based on a Monte Carlo simulation and using the Watson-Migdal ansatz [37] is even compatible with a pure $^1S_0$ interaction. A more quantitative analysis, however, requires a refined treatment of the FSI peaks taking into account a realistic ^{3}He wave function similar to the calculations of [38]. This is evident, since the simple Watson-Migdal matrix element overestimates the event density in the center of the Dalitz plot. Or vice versa, a consistent description of the density distribution in the Dalitz plot itself is sensitive to the ^{3}He wave function and especially to the details of the FSI enhancements. In any case, the transition probabilities $\Gamma(\pi NN \rightarrow NN)$ (see

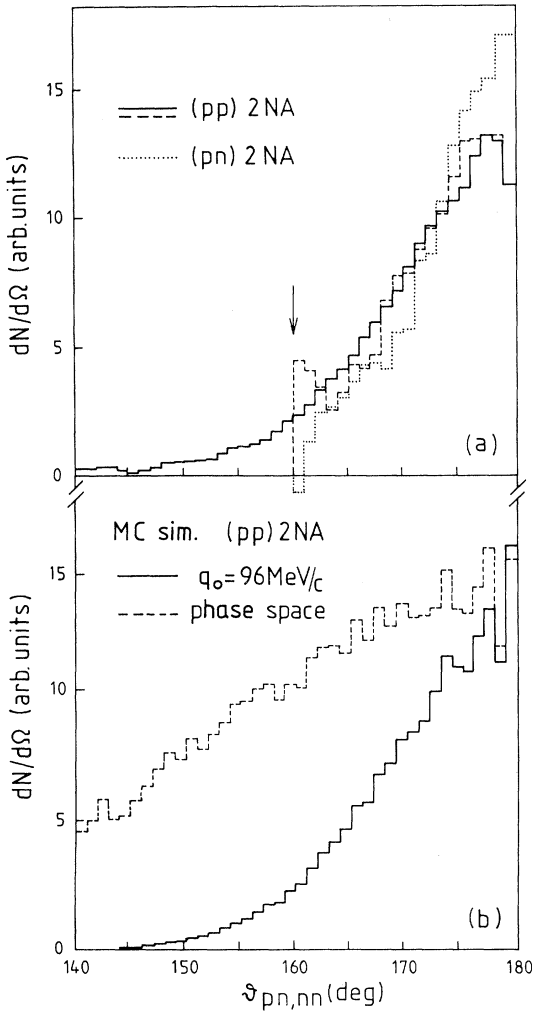

FIG. 17. (a) Measured opening-angle distributions of the 2NA regions. The intensities are normalized to the angular interval 165°–178°. ——, (*pp*)2NA setup I, width = (11±1)° (FWHM); – – –, (*pp*)2NA setup II, width =(11±3)° (FWHM); · · · ·, (*pn*)2NA setup II, width = (9±3)° (FWHM) (the arrow indicates the cut to the angular acceptance in setup II). (b) Monte Carlo simulation (MC sim.) to compare the opening angle distribution of the (*pp*)2NA region for correlated nucleon-nucleon emission and phase-space distributed events. The parameter q_0 is taken from the recoil momentum distribution (see Fig. 16).

Sec. V) can be better quantified by an evaluation of the 2NA regions.

In principle, it is possible to extract the various NN scattering lengths from the shape of the FSI distributions. Our measured distributions can be described with the values known from dedicated experiments [39,40]. However, the determination of values which are more accurate require better energy resolutions than achieved in this experiment.

The ratio of FSI(pn)/FSI(nn) is very close to the ratio $R(^3\mathrm{He}) = f^{(pn)2\mathrm{NA}}/f^{(pp)2\mathrm{NA}}$ (Table V) suggesting that the regions with final-state interaction are fed

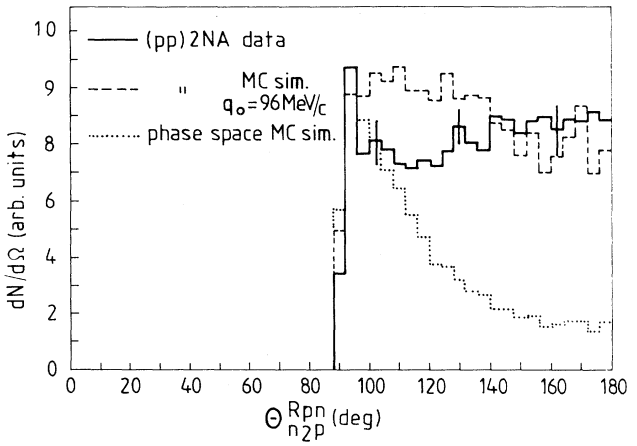

FIG. 18. Angular distribution of the recoiling neutron with respect to the absorbing *pp* pair, i.e., in the rest frame (Rpn_1) of the emitted *pn* pair (see Fig. 1). The errors are statistical only. The data are compared to Monte Carlo generated spectra for pure (*pp*)2NA absorption and pure phase space. The spectra are normalized to the same height at 90°. The small enhancements towards 180° might be attributed to FSI (see text). The deviation from isotropy seen in the Monte Carlo generated histogram for 2NA absorption is Rpn_1 due to the cut I3 (see Fig. 15). $\Theta^{Rpn_1}_{n2p} = 90°$ corresponds to $\Phi = 60°$.

by the 2NA channels. The two-particle final state *dn* may be regarded as a special case of the FSI(pn) final-state interaction leading to the $^3S_1$ two-nucleon bound state. The different K yields, however, of the *dn* and FSI final states are in contradiction to such a simple picture (see Table IV). The relative strength of the three-particle and two-particle final states is found to be $f^{pnn}/f^{dn} = 4.2 \pm 0.6$ in agreement with the result of Zaimidoroga *et al.*, which is 3.6 ± 0.6 [9].

D. Three-nucleon absorption

Statistical emission of three nucleons is attributed to three-nucleon absorption (3NA) [7]. We have searched for

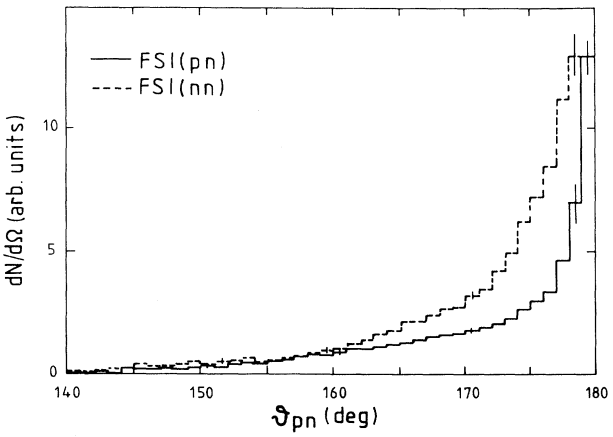

FIG. 19. Measured opening-angle distributions of the FSI regions. The vertical bars indicate the statistical errors.

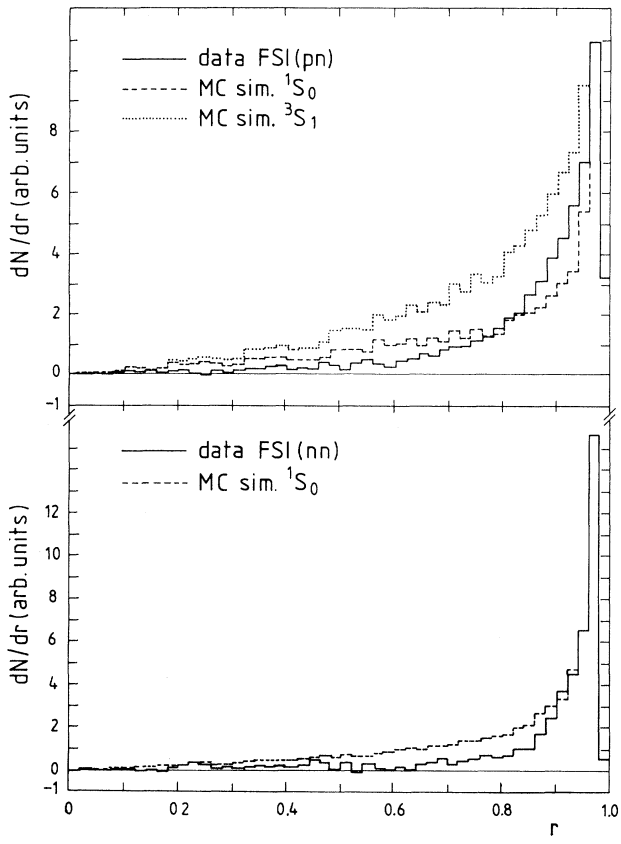

FIG. 20. r distributions of the FSI regions. For the Monte Carlo simulations, the Watson-Migdal ansatz was used [37], which overestimates the density at low r. For the scattering lengths a_{NN} and effective ranges r_{NN} we used $a^s_{pn} = 5.41$ fm, $r^s_{pn} = 2.67$ fm, $a^t_{pn} = -23.7$ fm, $r^t_{pn} = 1.75$ fm [39], $a^s_{nn} = -16.4$ fm, and $r^s_{nn} = 2.5$ fm [40]. The data are compatible with pure $^1S_0$ interaction.

a 3NA process in the data measured with setup I. In the Dalitz plot, this would show up as a constant contribution below the 2NA and the FSI populations. Therefore, the determination of a 3NA strength strongly depends on the tails of the 2NA and the FSI distributions.

The data of the (pp)2NA region were projected to the radius r of the Dalitz plot (Fig. 21). The comparison with a Monte Carlo generated spectrum suggests a negligible contribution from 3NA events. If all events with $r \leq 0.4$ are attributed to 3NA, an upper limit of 23% of (pp)2NA is obtained. As the branching ratio of (pp)2NA is 10.3% of the final state pnn, the upper limit is 5.5%

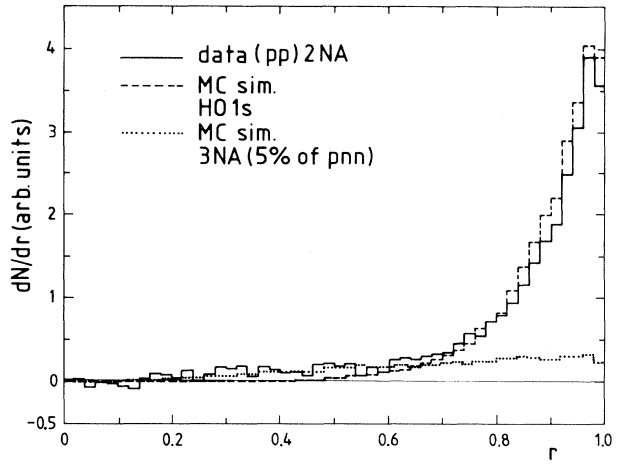

FIG. 21. Extraction of the upper limit for 3N absorption from the r distribution of the (pp)2NA region. ——, data as selected by cut I3 (Fig. 14); – – –, Monte Carlo generated spectrum of the (pp)2NA region; ($1s$ harmonic oscillator wave function with $q_0 = 96$ MeV/c). · · · · ·, 3NA corresponding to a 5% branching ratio of the final state pnn.

3NA for the final state pnn or $3\%/\pi^-_{\rm stop}$. In the Monte Carlo simulation, the tails of the FSI regions have not been taken into account and the branching ratio for 3NA can be regarded as a safe upper limit.

To determine the fraction of 3NA in the FSI regions, the long tails of the FSI peaks must be taken into account. One obtains upper limits for 3NA contributions to the final state pnn of 9% and 7% for the regions FSI(pn) and FSI(nn), respectively, if again all events with $r \leq 0.4$ are summed up. The Monte Carlo simulations show that the tails even exceed the values observed in the experiment for $r \leq 0.8$. As mentioned before (Sec. IV C), this is due to the very broad FSI peaks in the Watson-Migdal ansatz. Considering a more realistic model with smaller tails, the upper limits of $3\%/\pi^-_{\rm stop}$ for 3NA is justified.

E. Particle–x-ray coincidences

Our results from the measurement of the dn and pnn final states in coincidence with the pionic K x-rays are included in Tables IV and V. It is found that the relative intensities of the 2NA and FSI regions do not change significantly compared to the twofold coincidences. The quantities R and R_s, denoting the ratios for quasifree absorption on pn to pp pairs without and with the K x-rays measured in coincidence, are equal within the errors.

TABLE V. Measured ratios of quasifree absorption 2NA and FSI of the final state pnn. The bottom line shows the results obtained in coincidence with the pionic K x-rays. The ratios in the second column are defined to be $R(^3\text{He})$ and $R_s(^3\text{He})$, respectively.

	$\frac{(pn)\text{2NA}}{(pp)\text{2NA}}$	$\frac{\text{FSI}(pn)}{\text{FSI}(nn)}$	$\frac{(pn)\text{2NA}}{\text{FSI}(pn)}$	$\frac{(pp)\text{2NA}}{\text{FSI}(nn)}$	$\frac{\text{2NA}}{\text{FSI}}$
$\pi^-_{\rm stop}$ ^{3}He$\rightarrow pnn$	6.3 ± 1.1	5.7 ± 1.2	3.2 ± 0.6	3.2 ± 0.5	3.2 ± 0.4
$\pi^-_{\rm stop}$ ^{3}He$\rightarrow pnn \cdot X$	6.6 ± 2.5	8.6 ± 2.8	2.8 ± 1.1	4.1 ± 2.1	3.3 ± 1.4

The errors are dominated by the low statistics of the threefold coincidences.

In a separate experiment, the K yields Y_K (fraction of absorption from the atomic $1s$ state to absorption from all atomic states for a specific decay channel) had been determined for the final states pnn and dn to ≈ 0.3 and ≈ 0.5, respectively [28,29]. There, proton energies were limited to $T_p \geq 20$ MeV, i.e., the measurement covers only the regions FSI (pn), (pp)2NA, and FSI(nn). In our experiment, we find that also Y_K of the (pn)2NA process is ≈ 0.3. That means that the K yield of the three-particle final state is independent of the kinetic energy of the proton.

The difference in the K yields for the two- and three-particle final states is remarkable. The larger K yield of the dn channel corresponds to an enhancement for absorption from the atomic $1s$ level of the reaction π^-_{stop} ^{3}He$\rightarrow$ dn. This is reflected in a smaller value of the ratio $f^{pnn}_{1s}/f^{dn}_{1s} = 2.71 \pm 0.68$ for the absorption exclusively from atomic $1s$ states as compared to the value $f^{pnn}/f^{dn} = 4.2 \pm 0.6$ obtained from all atomic states. The high value of Y^{dn}_K suggests that there is no room left for dn emission from atomic p states. In principle, the reaction π^-_{stop} ^{3}He$\rightarrow$ dn should be favored from atomic s states, because of higher relative momenta for dn emission (i.e., smaller distances of the two absorbing subclusters) compared to NN emission, but no quantitative explanation exists up to now.

A similar enhancement of K yields was observed by Reich for pion absorption in Li isotopes for final states with composite particles [41]. It was found, that the K yield increases with the mass of the emitted particles. The K yields observed for the reactions π^-_{stop} ^{6}Li$\rightarrow$ tt and π^-_{stop} ^{7}Li$\rightarrow$ ttn (n being spectator) are larger by a factor of about 5 and 10, respectively, than for the quasifree (pp)2NA reaction.

F. Absorption from atomic s states versus p states and atomic cascade

The relative strength of absorption from atomic s and p states has been addressed already in the discussion of the K yield measurement of various π^-_{stop} ^{3}He decay channels by Backenstoss *et al.* [28]. In principle, it is possible to derive the ratio R_p (the analogue of R_s, but for absorption from all atomic p states) from the quantities R, R_s, and the branching ratio f^{pnn}_{ns} for pnn emission from all atomic s states. If we assume that there is no dependence on the principal quantum number n and that $f^{dn}_{ns} \approx f^{dn} = 0.130 \pm 0.015$ (see Table IV), we obtain

$$f^{pnn}_{ns} = (f^{pnn}_{1s}/f^{dn}_{1s}) f^{dn} \quad (n \geq 1) \qquad (9a)$$
$$= 0.35 \pm 0.10.$$

The result is consistent with the limits $f^{pnn}_{1s} = Y^{pnn}_K f^{pnn} < f^{pnn}_{ns} < f^{pnn}$ set by the K yield Y^{pnn}_K and the total branching ratio f^{pnn} of the three-body final state:

$$0.17 \pm 0.04 < f^{pnn}_{ns} < 0.55 \pm 0.07. \qquad (9b)$$

To calculate $R_p = f^{(pn)2\text{NA}}_{np}/f^{(pp)2\text{NA}}_{np}$, we use the following approximations:

$$R_s \approx R_{ns} = f^{(pn)2\text{NA}}_{ns}/f^{(pp)2\text{NA}}_{ns} \quad (n \geq 1),$$
$$f^{pnn} \approx f^{(pn)2\text{NA}} + f^{(pp)2\text{NA}},$$

and

$$f^{pnn}_{ns} \approx f^{(pn)2\text{NA}}_{ns} + f^{(pp)2\text{NA}}_{ns},$$

i.e., here, we make the assumption that the NN final-state interaction does not change the ratio for absorption on pn and pp pairs. With $R = f^{(pn)2\text{NA}}/f^{(pp)2\text{NA}}$ we obtain the equation

$$R_p = (f^{(pn)2\text{NA}} - f^{(pn)2\text{NA}}_{ns})/(f^{(pp)2\text{NA}} - f^{(pp)2\text{NA}}_{ns}).$$

Because $R \approx R_s$ and because f^{pnn}_{ns} is close to f^{pnn}, our results are not very sensitive to R_p and we can derive only an upper limit of

$$R_p < 18 \quad (90\% \text{ C.L.}). \qquad (10)$$

Additional information on the initial state comes from studies of the atomic cascade. A high-resolution measurement of pionic K x-rays from ^{3}He using a Si(Li) semiconductor detector and also at a target density corresponding to 60 bars at room-temperature reports for the hadronic $1s$ level width $\Gamma_{1s} = 28 \pm 7$ eV and $Y_K = (27 \pm 7)\%$ for the capture from the atomic $1s$ state [42]. For the hadronic $2p$ level width, the recent experimental result is $\Gamma_{2p} = (1.0 \pm 0.2)$ meV [43] (using $\Gamma^{\text{x}}_{2p} = 1.883$ meV for the radiative decay rate of the $2p$ level). A cascade model calculation of Landua and Klempt [44,45], which includes molecule-ion formation is able to reproduce the experimentally observed pressure dependence of the x-ray yields of muonic, pionic, and antiprotonic helium (without free parameters). From this calculation, $\Gamma_{2p} = 0.7 \pm 0.2$ meV was predicted for pionic ^{3}He. The total yield of absorption from all s states was predicted to be $(87 \pm 6)\%$ and $(13 \pm 6)\%$ for p states at a pressure of 60 bars. Combining these informations, the fractions of absorption from higher s states ($n \geq 2$) are $(60 \pm 9)\%$ and $(7 \pm 2)\%$ for the $2p$ level. The cascade analysis of Schwanner *et al.* [42], which follows the approach of Eisenberg and Kessler [46] obtains $(37 \pm 3)\%$ for s capture with $n \geq 2$ and $(31 \pm 7)\%$ for capture from all p levels. The cascade code used there, however, is not able to reproduce the pressure dependence of the x-ray intensities with one consistent set of parameters.

Taking into account that the branching ratios for charge exchange (3) and radiative capture (4) are negligible for absorption from the $2p$ state (5% only [47]) and assuming that $f^{dn}_{ns} \approx f^{dn}$, we can set $f^{pnn}_{np} = 0.13 \pm 0.06$ as obtained in the cascade calculation of Landua [44]. Using

$$1 = f^{pnn}_{ns} + f^{pnn}_{np} + f^{dn}_{ns} + f^{\pi^0 t}_{ns} + f^{\gamma t, \gamma dn, \gamma pnn}_{ns} \qquad (11)$$

we derive $f^{pnn}_{ns} = 0.46 \pm 0.07$ and $R_p < 27$ (90% C.L.), which is consistent with our results (9) and (10). The branching ratios for charge exchange and radiative cap-

ture were taken to be $f_{ns}^{\pi^0 t} \approx f^{\pi^0 t} = 0.135 \pm 0.023$ [28] and

$$f_{ns}^{\gamma t,\gamma dn,\gamma pnn} \approx f^{\gamma t,\gamma dn,\gamma pnn} = 0.140 \pm 0.012$$

[12].

From the ratio f_{ns}^{pnn}/f^{pnn} of our triple-coincidence measurement and independently from the atomic cascade, we conclude that the three-particle final state *pnn* is produced mainly by absorption from atomic *s* states. Therefore, our results from the twofold coincidences can at first order be interpreted as absorption from atomic *s* states. In other words, R is approximately equal to R_s.

V. DISCUSSION

The results from this experiment underline the dominance of the 2NA mechanism. This seems natural because single-nucleon absorption on a free nucleon is strictly forbidden by energy-momentum conservation and strongly suppressed when embedded into a nucleus. In the "quasideuteron" picture, a (bound) nucleon pair shares the pion rest energy and the nucleons experience a large momentum transfer of $k \approx 360$ MeV/c while the rest nucleus acts only as a spectator. "Quasifree" absorption, however, is distorted by initial- and final-state interactions involving nucleons not taking part in the genuine absorption process.

The ^{3}He nucleus is built up mainly of NN pairs with zero relative angular momentum. The wave function consists of a symmetric (S:≈ 90%) and an asymmetric *s*-wave (S':≈ 1–2%) and a *d*-wave part (D:≈ 8–9 %) [48,49]. The possible transitions $(NN)_i \rightarrow (NN)_f$ for NN pairs of the initial states $^1S_0$ and $^3S_1$ are listed in Table VI. The role of the $^3D_1$ neutron-proton pairs is discussed below.

Theoretically, pion absorption has been treated in the framework of the optical potential, effective coupling constants (for "deuteronic" transition strengths), *s*- and *p*-wave rescattering, and the isobar model (NN' and ΔN intermediate states). A compilation of theoretical results is given in Table VII. Almost all of these concepts use the 2NA picture originally introduced by Brueckner, Serber, and Watson [50]. An early calculation specific for ^{3}He was performed by Messiah in the impulse approximation which yields a reasonable value for the ratio of the pure absorption channels *pnn* (1) and *dn* (2) [51]. Cheon accounts for the 2NA mechanism by introducing NN pair short-range correlation functions of Gaussian type [52]. This approach underestimates both the ratio R and the transition rate by a factor of about 3.

The main topic of our discussion is the ratio $R(^3\mathrm{He}) = f^{(pn)2\mathrm{NA}}/f^{(pp)2\mathrm{NA}}$ which is closely related to the ratio of absorption on isoscalar to isovector NN pairs. To compare results for ^{3}He to other nuclei, a statistical factor $2N/(Z-1)$ for the ratio of initial *pn* to *pp* pairs of a nucleus $A(Z,N)$ must be taken into account. The statistical factor is approximately equal for ^{3}He, $N = Z$ nuclei, and average nuclear matter except for light nuclei like ^{4}He and ^{6}Li.

A. Phenomenological optical potential

In the optical potential approach, 2NA is parametrized by the quantities $\mathrm{Im}B_0$ and $\mathrm{Im}C_0$ for *s*- and *p*-wave absorption, respectively:

$$\mathrm{Im}U_{\mathrm{opt}} = -\frac{4\pi}{2\omega}\rho^2(r)(\mathrm{Im}B_0 + \vec{k}^2\mathrm{Im}C_0) \ . \qquad (12)$$

$\mathrm{Im}B_0$ and $\mathrm{Im}C_0$ are determined from fits to low-energy pion-nuclear cross sections and pionic atom data. ω and $\vec{k}$ are the total energy and momentum of the pion. The quadratic dependence in the nucleon density, $\rho(r)$, accounts for the absorption on a pair of (uncorrelated) nucleons. As the absorption depends on the isospin I of the absorbing NN pair, the parameters separate into

$$\mathrm{Im}B_0 = \mathrm{Im}B_0(I=0) + \mathrm{Im}B_0(I=1)$$

and

$$\mathrm{Im}C_0 = \mathrm{Im}C_0(I=0) + \mathrm{Im}C_0(I=1),$$

respectively. Fits to the isoscalar and isovector parts sep-

TABLE VI. Transitions of *s*-wave NN pairs of state $^{2I+1,2S+1}L_j$ for *s*- and *p*-wave pion absorption allowed by isospin, parity, and angular-momentum conservation; relation of effective coupling constants g_i and γ_i (column 5) to the parameters $\mathrm{Im}B_0$ and $\mathrm{Im}C_0$ (column 6) of the optical potential. For *p*-wave pions, the extended Pauli principle allows the transitions $^{31}S_0 \rightarrow {}^{13}S_1 + {}^{13}D_1$ only for initial *pp* pairs. The possible NN' and $N\Delta(1232)$ intermediate states are given in columns 3 and 4. The various total spins (if existing) are separated by commas: S = total spin, L = orbital angular momentum, j = total angular momentum, I = isospin.

	$(NN)_i \rightarrow (NN)_f$	NN'	$N\Delta$	Eff. coupling constant	Opt. potential parameter	Involved nucleons
$l_\pi = 0$	$^{13}S_1 \rightarrow {}^{33}P_1$	$^{31,3}P_1$	$^{33,5}P_1, {}^{35}F_1$	$\lvert g_o\rvert^2$	$\mathrm{Im}B_0(I=0)$	$pn \rightarrow nn$
	$^{31}S_0 \rightarrow {}^{33}P_0$	$^{33}P_0$	$^{33}P_0$	$\lvert g_1\rvert^2$	$\mathrm{Im}B_0(I=1)$	$pp \rightarrow pn, pn \rightarrow nn$
$l_\pi = 1$	$^{13}S_1 \rightarrow {}^{31}S_0$	$^{31}S_0$	$^{35}D_0$	$\lvert\gamma_3\rvert^2 = \gamma_{01}$		
					$\mathrm{Im}C_0(I=0)$	$pn \rightarrow nn$
	$\rightarrow {}^{31}D_2$	$^{31}D_2$	$^{35}S_2, {}^{33,5}D_2, {}^{35}G_2$	$\lvert\gamma_4\rvert^2 = \gamma_{21}$		
	$^{31}S_0 \rightarrow {}^{13}S_1, {}^{13}D_1$	$^{13}S_1, {}^{13}D_1$		$\lvert\gamma_1+\gamma_2\rvert^2 = \gamma_{10}$	$\mathrm{Im}C_0(I=1)$	$pp \rightarrow pn$

TABLE VII. Compilation of theoretical results compared to experimental results for π^-_{stop} ^{3}He. The experimental results are understood to be a good approximation for s-wave absorption. IA, impulse approximation; 2NA, two-nucleon absorption; FSI, nucleon-nucleon final-state interaction; SRC, short-range correlation; mod. IG, modified Irving-Gunn wave function.

$\lvert g_0\rvert^2$ (fm^8)	$\lvert g_1\rvert^2$ (fm^8)	$\lvert g_0/g_1\rvert$	$\frac{(pn)2NA}{(pp)2NA}$ $l_\pi = 0$	$\frac{(pn)2NA}{(pp)2NA}$ $l_\pi = 1$	$\frac{pnn}{dn}$	Γ_{1s}^{pnn+dn} (eV)	Remark	Ref.
					2.7 ± 0.9		Weak πN coupling, IA	[51][a]
0.32 ± 0.04	0.29 ± 0.15	1.1 ± 0.6	~ 1.6		4.6 ± 4.1	5.2 ± 1.9	Zero-range 2NA; Gaussian wave function; g_0, g_1 from [59], $g_0 g_1 > 0$	[60][a]
			3.4 ± 1.4	2.0 ± 0.8			B_0, C_0; opt. potential from πN and	[57][a]
			4.1 ± 1.2	7.8[f]			$NN \rightleftharpoons NN\pi$ cross sections	[57][b]
			1.27		6.93	7.1	πN interaction, NN pair correlation and SRC 0.55 fm^{-2}	[52][a]
			3.7 ± 0.9				s-wave rescattering (scaled from π^- ^{4}He)	[78]
0.64 ± 0.05	0.155 ± 0.08	2.03 ± 0.26	4.6 ± 1.2	5	1.9	8.5	Zero-range 2NA; Gaussian wave function;	[63][a]
0.48 ± 0.01	0.136 ± 0.04	1.88 ± 0.08	4.0 ± 0.4				$g_0 g_1 > 0$	[63][b]
0.48	0.31	1.24	$3 - 12$	~ 4	2.3	26.1	2NA; mod. IG wave function; $g_0 g_1 > 0$	[61][a]
20.55	8.46	1.56	3.1	~ 7.9	3.5 ± 0.4	27 ± 6	2NA; exp. III, range 0.6 fm; $g_0 g_1 > 0$	[64][a]
			$\simeq 3$				Rescattering; off-shell πN amplitudes	[80]
			9.3	7.2–15			Rescattering; NN correlations	[85]
2.44	2.27	2.04 ± 0.49	4.7		2.7	16.1	2NA, FSI; abs. range 0.6 fm; $g_0 g_1 > 0$ and	[38][a]
6.84		1.74 ± 0.44	3.5				Hulthén wave function for ^{3}He	[38][b]
			8.7				p_{11} and Δ isobar interference	[90]
			~ 4				Rescattering; Δ and N intermediate states with extrapolation to $T_\pi = 0$	[92]
9.17	2.35	2 ± 1	4.4		3	20.7	2NA, FSI, Hulthén wave function	[62] [a]
6.65	2.35	1.7 ± 0.6	3.8 ± 2.1		$2.2 - 3.9$		absorption range 0.6 fm	[62][b]
			~ 3		3.6 ± 0.6		Experiment: 17.5 bars ^{3}He	[9]
		2.48 ± 0.24[c]	6.3 ± 1.1	< 40	4.24 ± 0.62	15.3 ± 4.3[d]	Experiment: 60 bars ^{3}He	This
						19.7 ± 5.7[e]		experiment

[a]Specific calculations for the ^{3}He nucleus.
[b]Original results scaled with recent $NN \rightleftharpoons NN\pi$ cross section data [65–67].
[c]With the cluster model used by [68].
[d]With $\Gamma_{1s} = 28 \pm 7$ eV [40] and with the K yields $Y_K^{dn} = 0.47$, $Y_K^{\pi^0 t} = 0.35$, and $Y_K^{\gamma} = 0.35$ from [28].
[e]As [d] but with $Y_K^{\gamma} = 1$ from [28].
[f]From [58].

arately are not unambiguous and even contradictory in the various analyses, especially for light nuclei [53–56].

Ericson and Ericson built up $\mathrm{Im}B_0$ and $\mathrm{Im}C_0$ from the "deuteronic strength" parameters $\mathrm{Im}\beta_{jt_1}(l_\pi = 0)$ and $\mathrm{Im}\gamma_{jt_1}(l_\pi = 1)$ for the absorption on s-wave NN pairs [57]. The indices denote total spin j and isospin t_1 of the πNN system. $\mathrm{Im}\beta_{jt_1}(l_\pi = 0)$ and $\mathrm{Im}\gamma_{jt_1}(l_\pi = 1)$ are related to the transition rates $\Gamma(\pi NN \to NN)$ for nucleon pairs with the corresponding quantum numbers and have been derived phenomenologically from low-energy pion-production experiments. The ratios of nn to pn emission for s- and p-wave pions are

$$R_s = 3\ \mathrm{Im}\beta_{11}/\mathrm{Im}\beta_{01} + 1\ , \tag{13a}$$

$$R_p = \mathrm{Im}(\gamma_{01} + 5\gamma_{21})/\mathrm{Im}\gamma_{10}\ . \tag{13b}$$

This ansatz yields $R_s = 4.1 \pm 1.2$ when $\mathrm{Im}\beta_{jt_1}$ is scaled with recent results for the $NN \leftrightarrow NN\pi$ cross sections (see Table VII) and $R_p = 7.8$ using the values given in [58].

B. Effective coupling constants

Eckstein introduced the effective coupling constants g_0 and g_1 for absorption of s-wave pions on s-wave NN pairs [59] (similar phenomenological constants have been defined for p-wave absorption [60,61]). The coupling constants are determined from low-energy $NN \leftrightarrow NN\pi$ cross sections and contain inherently the short-range correlation of the absorbing NN pair and the (zero or finite) range of the specific $NN \leftrightarrow NN\pi$ reaction. The experimental information mainly stems from the reactions $pp \leftrightarrow d\pi^+(g_0)$ and $pp \to pp\pi^0(g_1)$. The indices of g_0 and g_1 are related to the isospin changing ($I = 0 \to I' = 1$) and nonchanging ($I = 1 \to I' = 1$) transitions of the nucleon pair (see Table VI). Neglecting interference terms, the ratio of absorption on pn to pp pairs is given by

$$R_s(^3\mathrm{He}) = |g_0/g_1|^2 + \tfrac{1}{2}\ . \tag{14}$$

Equation (14) is identical to Eq. (16) in [62], but there $np \to nn$ and $pp \to nn$ must be interchanged. With the experimental values from Table VII one obtains $|g_0/g_1| = 2.41 \pm 0.23$ from R and 2.47 ± 0.51 from R_s. (According to the discussion in Sec. IV F, R is understood to be a good approximation for R_s.) Theoretically, various wave functions, NN correlations, and absorption functions describing the range of the πNN interaction have been discussed for the case of ^{3}He (see [38,60,62–64] in Table VII). The choices of a Hulthén wave function and an interaction range of ≈ 0.6 fm seems to be most suitable for describing the data. The interaction range of 0.6 fm perfectly fits the relative momentum of the two nucleons after absorption. The ratio R_s, however, is underestimated at least by a factor of ≈ 1.6 in these calculations. Note that some of the calculations for $|g_0/g_1|$ collected in Table VII have been scaled according to the results from the recent $NN \leftrightarrow NN\pi$ experiments [65–67].

The ratio R_s as given by Germond and Wilkin (Eq.(4.2) in [68]) includes the D-wave contribution of the NN pairs in the ^{3}He nucleus

$$\frac{R_s(^3\mathrm{He}) = (c_{^3S_1} + c_{^3D_1})|g_0|^2 + \frac{1}{2}c_{^1S_0}|g_1|^2}{c_{^1S_0}|g_1|^2} \tag{15}$$

[compare to the approximation (14)]. The coefficients $c_{^{2S+1}L_j}$ are the fractions of two-body clusters in the initial state $^{2S+1}L_j$ and were taken from variational wave-function calculations for the ^{3}He nucleus ($c_{^3S_1} = 1.32$, $c_{^3D_1} = 0.022$, $c_{^1S_0} = 1.42$ [68]). From the experimental value $R = 6.3 \pm 1.1$, we obtain

$$|g_0/g_1| = 2.48 \pm 0.24. \tag{16}$$

Using the value $R_s = 6.6 \pm 2.5$, the result is $|g_0/g_1| = 2.54 \pm 0.52$. Relation (15) is displayed in Fig. 22 as a function of the ratio g_0/g_1. Included in the upper part of the figure are three results for g_0/g_1 based on the analysis of Roginsky and Werntz [62], indicated by 3 bars with two arrows each. The top bar is obtained from $R = 6.3 \pm 1.1$ and (14). The middle bar is the value for g_0/g_1 deduced by Roginsky and Werntz, but scaled with recent results of $NN \leftrightarrow NN\pi$ experiments (see Table VII). The large error stems from the uncertainty of g_0, i.e., the $pp \to pp\pi^0$ cross section at threshold and is caused by the lack of a detailed analysis including the Coulomb final-state interaction of the protons but not from the accuracy of the data. The bottom bar is obtained using the ratio $f^{pnn}/f^{dn} = 4.2 \pm 0.6$ from this experiment.

Assuming time-reversal invariance, the ratio g_0/g_1 is almost real [59]. The relative sign of g_0 and g_1 can be determined from the ratio f^{pnn}/f^{dn}. Most of the calculations predict that the branching ratio f^{dn} of the two-body final state decreases by a factor of about 3 if $g_0 g_1 < 0$ is chosen, whereas the branching ratio f^{pnn} of the three-body state is little affected. The result from this experiment suggests $g_0 g_1 > 0$ in agreement with earlier analyses [38,62,64,68,69]. The situation, however, is contradictory, because Figureau and Ericson obtain better agreement with data for $g_0 g_1 < 0$ [63]. In Table VII, all the predictions for the transition rates Γ_{1s}^{pnn+dn} (absorption from the atomic $1s$ state leading to the final states pnn and dn) are given for the positive phase of g_0 and g_1. The error of the experimental value is dominated (i) by the uncertainty of the $1s$ level width (25%) [42] and (ii) the poor knowledge of the K yield for radiative capture (30–100%) [28].

The measured branching ratio f^{dn} for π^-_{stop} ^{3}He$\to dn$ is reproduced better, when the D-state contribution is taken into account [68]. The importance of S' and D waves was demonstrated already for the radiative pion capture in ^{3}He by Phillips and Roig [47]. Using the recent data for $\sigma(\pi^+ d \to pp)$ of Ritchie *et al.* [67] instead of the results from the analysis of Rose [70] and the ratio g_0/g_1 from this work, the values of the coupling constants in the work of Germond and Wilkin [68] change to $|g_0| = (4.6 \pm 0.1) \times 10^{-2}$ fm^2 and $|g_1| = (1.9 \pm 0.2) \times 10^{-2}$ fm^2. With these values, however, the result of [68] for f^{dn} decreases from 11.3 to 8.4 %, which is $\frac{2}{3}$ of our result of (13.0 ± 1.5)%. Again, g_0 and g_1 should be in phase,

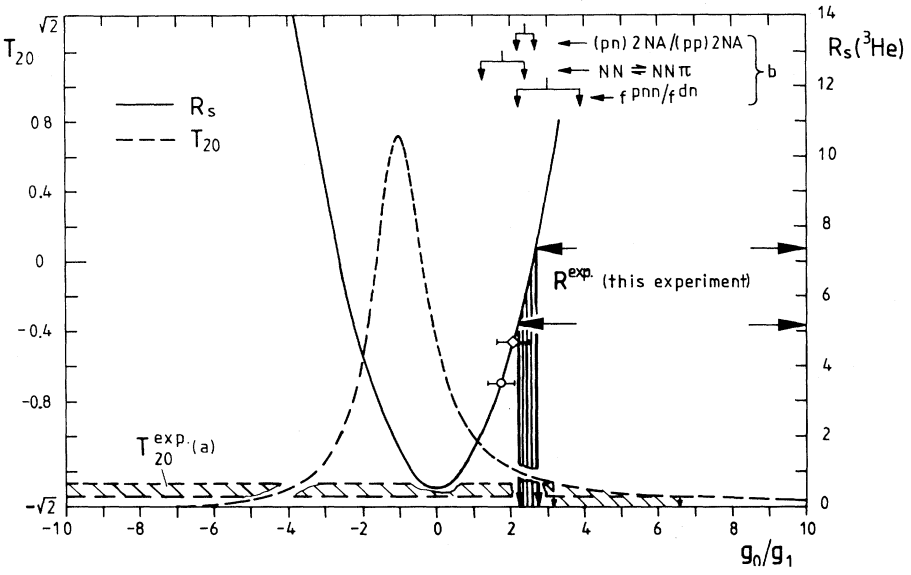

FIG. 22. Ratio $R = f^{(pn)2NA}/f^{(pp)2NA}$ and tensor analyzing power T_{20} as a function of the ratio of coupling constants g_0/g_1. The curves for R_s and T_{20} are calculated according to Germond and Wilkin (Eqs. (4.2) and (3.11) of [68]) including the ^{3}He D-wave contribution. Only the positive phase between g_0 and g_1 is considered in the comparison with the data. *a*, measurement of T_{20} with the reaction $p\vec{d} \rightarrow {}^3\mathrm{He}\pi^0$ [72]; *b*, analysis according to Roginsky and Werntz for g_0/g_1 [62]: top, using R from this experiment and Eq. (14); middle, using recent $NN \leftrightarrow NN\pi$ cross sections [65,67] (see text); bottom, using $f^{pnn}/f^{dn} = 4.2 \pm 0.6$ from this experiment; ◇, calculation of Nägeli [38] using g_0 and g_1 as determined form previous $NN \leftrightarrow NN\pi$ experiments; ○, as ◇, but scaled according to the recent experimental results for $NN \leftrightarrow NN\pi$ cross sections [65,67].

because for $g_0 g_1 < 0$, f^{dn} decreases to 3% only.

Additional information about the ratio g_0/g_1 comes from measurements of the tensor analyzing power T_{20} in the reaction $\vec{d}p \rightarrow {}^3\mathrm{He}\pi^0$. The relation between T_{20} and g_0/g_1 is also displayed in Fig. 22 (Eq. (3.11) of [68]). For $g_0/g_1 = +2.48 \pm 0.24$, we obtain $T_{20} = -1.23 \pm 0.04$. Neglecting the D-state contribution to the ^{3}He wave function, the result is $T_{20} = -1.10 \pm 0.04$ (Eq. (3.16) in [68]). The experimental results are $T_{20}(\vec{d}p \rightarrow {}^3\mathrm{He}\pi^0) = -1.05 \pm 0.15$ [71] (extrapolation to threshold from higher energies) and -1.31 ± 0.04 [72] (measurement at threshold). The value of T_{20} from the threshold measurement is included in Fig. 22. It is close to the result from π^- absorption in ^{3}He for the positive phase between g_0/g_1.

Various rate estimates exist for the absorption of p-wave pions. The results, however, spread widely. Mostly, $R_p \approx (2\text{–}3)R_s$ is predicted yielding $R_p \approx 4\text{–}15$ [57,58,60,61,63,64]. As discussed in Sec. IV F, our data are hardly sensitive to R_p.

C. Rescattering mechanism

At low energies, the s- and p-wave rescattering mechanism provides a microscopic picture of pion absorption on two nucleons. In this model, the pion is scattered (on shell or off shell) at the first nucleon and absorbed by the second one. The dynamics of the absorption is governed by the low-energy πN scattering amplitudes and to a lesser extent by the πNN vertex. The model has been used successfully to describe the disintegration of the deuteron [73–76].

Introducing s-wave rescattering, Koltun and Reitan found $R_s \approx 9$ for π^- ^{16}O and $R_s = 7.4 \pm 1.8$ for π^- ^{4}He which scales to $R_s = 3.7 \pm 0.9$ for π^- ^{3}He [77,78]. The suppression of the $\pi^- pp \rightarrow pn$ channel is explained by its small rescattering contribution which traces back to the smallness of the isospin even combination of the (on-shell) πN scattering lengths.

In a rigorous treatment in terms of πN scattering and the πNN vertex, Hachenberg, Hüfner, and Pirner studied for pion absorption on uncorrelated NN pairs the dependence on the off-shell behavior of the πN amplitudes [79,80]. They obtained $R_s = 3$ using the off-shell amplitudes and the unrealistic value of $R_s \approx 100$ for the on-shell πN amplitudes. With our value of 6.3 ± 1.1 for $R \approx R_s$ and Eq. (3.21) of [80], we obtain a $a^-/a^+ = 1.31 \pm 0.17$ for the ratio of the isospin-odd to the isospin-even off-shell pion-nucleon scattering amplitudes. This corresponds to an off-shell momentum of $|\vec{k}| \approx 220 \pm 10$ MeV/c which is between the on-shell ($a^-/a^+ = -13.9$ at $k = 0$) and the "absorption" or off-shell point $a^-/a^+ = 0.002$ at $|\vec{k}| = 360$ MeV/c. For $|\vec{k}| = 220 \pm 10$ MeV/c, we obtain $\mathrm{Im}B_0 = (0.012 \pm 0.002) m_\pi^{-4}$ from (3.23) of [80] (there is a second solution for $a^-/a^+ = 0.31 \pm 0.17$, which yields the limits $|\vec{k}| > 420$ MeV/c and $\mathrm{Im}B_0 > 0.05$, but is beyond the absorption point). From the lightest pionic atoms, smaller values for $\mathrm{Im}B_0$ are derived ($\mathrm{Im}B_0 = 0.029 m_\pi^{-4}$ for π^- ^{4}He [53]) as compared to the results for average "nuclear matter" [$\mathrm{Im}B_0 = (0.042 - 0.055) m_\pi^{-4}$ [53,56]]. In the case of deuterons with only one $^3S_1(I = 0)$ NN pair, $\mathrm{Im}B_0$ is as small as $(0.016\text{–}0.018) m_\pi^{-4}$ [58,81].

For nuclear matter, Efrosinin *et al.* obtain $R_s \approx 10$ and $\mathrm{Im}B_0 \approx 0.043 m_\pi^{-4}$ but introduce, in addition to the off-shell behavior, medium corrections by renormalizing meson-nucleon vertices [82]. In general, calculations or s-wave rescattering underestimate $\mathrm{Im}B_0$ by $\approx 30\%$ [74,83]. Medium corrections enhance the absorption rate close to the empirical value for average "nuclear matter" [82,84], which, however, deviate by a factor of about 2 from the absorption rate for π^- He.

In an alternative approach to the description with off-shell amplitudes, Shimizu and Faessler use recoil terms and NN short-range correlations assuming absorption on uncorrelated nucleons [76,85]. For p-wave absorption, a significant contribution from Δ rescattering is calculated. In this model, $R_s = 9.3$, $R_p = 7$–15, and $\mathrm{Im}B_0 = 0.033 m_\pi^{-4}$ are obtained.

In a forthcoming paper, Kiang, Lee, and Riska point to the importance of heavy-meson exchanges [86]. The effect of heavy-meson exchanges is to enhance the transition rate for the $pp \to pp\pi^0$ reaction [87], which in turn decreases the value for R_s. Including σ, ω, δ, and ρ exchange, $R_s \approx 9$ is predicted, whereas R_s increases to 530 if only pion rescattering is taken into account.

D. Isospin transition probabilities

In terms of reduced isospin transition rates $\Gamma_{II'}$ (I and I' are the isospins of the initial and final two-nucleon state), the ratio of nn to pn emission is given by

$$(pn)2\mathrm{NA}/(pp)2\mathrm{NA} = (\alpha\tfrac{1}{4}\Gamma_{11} + \beta\tfrac{1}{2}\Gamma_{01})/\gamma(\tfrac{1}{4}\Gamma_{11} + \tfrac{1}{6}\Gamma_{10}) \ . \quad (17)$$

The numerical coefficients are the Clebsch-Gordan coefficients of the isospin decomposition. The coefficients α, β, and γ account for the cluster decomposition of the absorbing nucleus into NN pairs of isospin 0 [α : $^3S_1(pn)$] and 1 (β : $^1S_0(pn)$, γ : $^1S_0(pp)$). The extended Pauli principle requires $\Gamma_{10} = 0$ for $l_\pi = 0$ and $\Gamma_{11} = 0$ for $l_\pi = 1$. Thus, for ^{3}He the nn to pn ratios for s- and p-wave pion absorption on s-state NN clusters are

$$R_s(^3\mathrm{He}) = 3\Gamma^s_{01}/\Gamma^s_{11} + \tfrac{1}{2} \ , \quad (18a)$$

$$R_p(^3\mathrm{He}) = \frac{9}{2}\Gamma^p_{01}/\Gamma^p_{10} \ . \quad (18b)$$

The coefficients α, β, and γ are taken to be the statistical ones ($\alpha = \frac{1}{2}$, $\beta = \frac{3}{2}$, $\gamma = 1$). The comparison of (14) and (18a) gives $|g_0/g_1|^2 = 3\Gamma^s_{01}/\Gamma^s_{11}$. From the experimental result of $R(^3\mathrm{He})$ we obtain for the ratio of the (s-wave) transition strength

$$\Gamma_{01}/\Gamma_{11} = \tfrac{1}{6}[2R(^3\mathrm{He}) - 1] = 1.93 \pm 0.37 \ . \quad (19)$$

With R_s as obtained from the measurement with triple coincidences, the result is $\Gamma_{01}/\Gamma_{11} = 2.03 \pm 0.83$.

E. Isobar intermediate states

In the isobar model, the pion coupled to the NN pair forms an intermediate NN' or $N\Delta$ state [88–92] (see Table VI). At threshold, the excitation of Δ and N' isobars is expected to be suppressed owing to the large mass mismatch. So, the N' is rather understood to be a ^{11}P πN interaction than a resonance [90]. On the other hand, the importance of p waves in the pion-nucleon interaction is well known even very close to threshold. Hence, the gradient term in the optical potential is necessary to describe the level shifts and broadenings in pionic atoms [3,57]. The measurements on pion absorption on deuterium of Hutcheon *et al.* and Ritchie *et al.* indicate p-wave contributions even at lowest energies [66,67] and Pickar *et al.* found strong constructive interference of s and p waves for pion emission at threshold for the reverse reaction $^2\mathrm{H}(\vec{p},\pi^0)^3\mathrm{He}$ [93].

The transition strengths in the isobar model are (without interference terms) [94]

$$\begin{aligned} \Gamma_{01} &= \tfrac{1}{3}(\Gamma_{N'} + 2\Gamma_\Delta) \ , \\ \Gamma_{11} &= \tfrac{1}{3}(2\Gamma_{N'} + \Gamma_\Delta) \ , \\ \Gamma_{10} &= \Gamma_{N'} \ . \end{aligned} \quad (20)$$

For Δ dominance ($l_\pi = 1$) the isospin ratio is $\Gamma_{01}/\Gamma_{11} = 2$, which corresponds to $R = \frac{13}{2}$. N' dominance ($l_\pi = 0$) results in $\Gamma_{01}/\Gamma_{11} = \frac{1}{2}$ or $R = 2$. Our result (19) suggests strong evidence for the Δ-isobar coupling being the main reaction mechanism. This is in contradiction to the naive s-wave absorption picture, because the amplitude $\pi N \to \Delta$ is zero for zero relative momentum of the pion and the nucleon. The calculation of Silbar and Piasetzky [90] requires an interference of NN' and $N\Delta$ intermediate states to reproduce the isospin ratio. Maxwell and Cheung [92] include both rescattering through Δ and nucleon intermediate states and s-wave rescattering as introduced in [77]. An extrapolation to threshold yields $R \approx 4$ (see Table VII).

In the case of negligible N' excitation, the transition rate Γ_Δ determines the cross sections and in the ratio R_s, the absolute value of the Δ-channel transition strength cancels. As mentioned before, this may cause the significant decrease of $\mathrm{Im}B_0$ for light pionic atoms, decreases the absorption cross section, and leads to a relative enhancement of the channel $\pi^- pp \to pn$ and the FSI peaks.

An angular momentum $l_\pi = 0$ of the pion with respect to the ^{3}He nucleus does not always require $l_\pi = 0$ with respect to the absorbing NN pair. For example, Divakaran has calculated that for $l_\pi = 1$ with respect to the ^{3}He nucleus, the ratio of the transition probabilities for the pion being in an s state or a p state to the absorbing NN pair to be 1.1 [60]. So, the high-momentum components of the wave function are important for theoretical calculations.

In ^{3}He, for pion absorption in flight, the energy dependence of the isoscalar cross section is found to be the same as for absorption in deuterium. This is explained by the Δ mechanism because the contribution with $l_\pi = 1$ and the $^5S_2(\Delta N)$ intermediate state from $^3S_1(I = 0)$

pair absorption dominates [91,95]. The energy dependence for isovector absorption is much less pronounced, because the ΔN intermediate state is forbidden in the case of $I = 1$ pairs and $l_\pi = 1$. For $l_\pi = 0$, the dominant intermediate state $^5S_2(\Delta N)$ cannot be reached. Both for isospin 0 and 1 NN pairs, intermediate ΔN or NN' states are in the nonfavored p wave, but not forbidden.

For photoabsorption in ^{3}He, the dominance of absorption on $I = 0$ NN pairs was also observed [96]. The suppression of absorption on pp pairs is explained like for pion absorption with the unfavorable spin and parity configuration for possible ΔN intermediate states. Close to threshold and especially for the weak channel of absorption on isovector NN pairs, a subtle interference behavior seems to occur between direct production and rescattering through s and p waves, which complicates the quantitative description considerably [95,97].

F. Multinucleon absorption and collective effects

At rest, no genuine three-nucleon absorption leading to the pnn final state has been observed with an upper limit of $3\%/\pi^-_{\rm stop}$. For stopped pions, the multinucleon process is strongly suppressed also in heavier nuclei such as ^{6}Li [98], but already amounts to $\approx 20\%$ in ^{3,4}He at $T_\pi = 65$ MeV [5,7,99]. Also for $E_\gamma = 200$ MeV in photoabsorption, which corresponds to the same center-of-mass Q value [see (6c)] as for pion absorption at $T_\pi = 64$ MeV, a sizable contribution of the three-body mechanism has been found [96]. No data are available for $E_\gamma \approx 142$ MeV, which corresponds to the Q value for the reaction $\pi^-\,^3\mathrm{He} \rightarrow pnn$. Up to now, there is no clear picture of the origin of phase-space distributed multinucleon final states.

Pion absorption on subclusters has been observed at rest [98,100]. Such collective effects in nuclei are being investigated also by inverse reactions like subthreshold particle production. In general, the number of nucleons involved increases with the mass of the absorbing nucleus [5,7,101]; similarly secondary and multistep processes may become more and more important [102]. For a satisfactory description, the final states have to be treated coherently, because final-state interactions mix with composite particle emission. The branching ratios in light nuclei cannot be explained by sequential reaction mechanisms like, e.g., pickup, as has been shown for the case of $\pi^-\,^6$Li by Dörr *et al.* [98].

In the case of ^{3}He, both one-nucleon absorption and the FSI configuration including the dn final state are kinematically identical. Due to the mass ratio of 2:1 between the "rest nucleus," the deuteron, and the "emitted" neutron, the momentum of the emitted nucleon is only $k \approx 415$ MeV/c. This momentum configuration is less suppressed as compared to the case of heavier nuclei where $k \approx 515$ MeV/c. Branching ratios for single-nucleon emission have been reported to be of the order of a few per mille [103,104], 2 orders of magnitude less than for the dn channel.

VI. CONCLUSION

It has been found that at threshold negative pions are dominantly absorbed on the isospin 0 NN pairs of the ^{3}He nucleus. A nucleon-nucleon final-state interaction, however, results in a considerable branching ratio for the two-particle final state dn and for unbound but correlated pn and nn pairs. No evidence is found for a genuine three-nucleon absorption with a statistical emission of all three nucleons. The density distribution of the Dalitz plot is reasonably well reproduced by calculations assuming two-nucleon absorption including final-state interaction. A thorough treatment including a realistic ^{3}He wave function and taking the final-state interaction coherently into account is indispensable for a quantitative description.

For the ratio of the effective coupling constants g_0/g_1, an overall agreement is obtained with results from tensor analyzing power and threshold pion production measurements. For the ratio R of absorption on isospin 0 to isospin 1 NN pairs, the theoretical predictions spread widely and deviate by factors of 0.2–2 from the experimental result. A better agreement within 50% is obtained from specific calculations for ^{3}He using the effective coupling constants g_0 and g_1 and Hulthén wave functions. The best agreement with the experimental result is obtained for isobar-nucleon intermediate states assuming Δ dominance, although the ΔN intermediate states should be suppressed for s-wave absorption.

ACKNOWLEDGMENTS

The authors would like to thank the PSI staff for the support of this experiment, H. Krause for the valuable technical assistance, K.-P. Wieder for his help with the numerous drawings, and L. Simons for his help during the early stage of the experiment. This work was supported in part by the German Bundesministerium für Forschung und Technologie and the Swiss National Science Foundation.

[1] J. Hüfner, Phys. Rep. **21**, 1 (1975).
[2] D. A. Ashery and J. P. Schiffer, Annu. Rev. Nucl. Part. Sci. **36**, 207 (1986).
[3] T. E. O. Ericson and W. Weise, *Pions and Nuclei* (Clarendon, Oxford, 1988).
[4] H. J. Weyer, Phys. Rep. **195**, 295 (1990).
[5] M. Steinacher, G. Backenstoss, M. Izycki, P. Salvisberg, P. Weber, H.-J. Weyer, A. Hoffart, B. Rzehorz, H. Ullrich, M. Dzemidzić, M. Furić, and T. Petković, Nucl. Phys. A **517**, 413 (1990).
[6] S. Mukhopadhyay, S. Levenson, R. E. Segel, G. Garino, D. Geesaman, J. P. Schiffer, G. Stephans, B. Zeidman, E. Ungricht, H. Jackson, R. Kowalczyk, D. Ashery, E. Piasetzky, M. Moinester, I. Navon, L. C. Smith, R. C.

Minehart, G. S. Das, R. R. Whitney, R. McKeown, B. Anderson, R. Madey, and J. Watson, Phys. Rev. C **43**, 957 (1991).
[7] P. Weber, G. Backenstoss, M. Izycki, R. J. Powers, P. Salvisberg, M. Steinacher, H. J. Weyer, S. Cierjacks, A. Hoffart, B. Rzehorz, H. Ullrich, D. Bosnar, M. Furić, T. Petković, and N. Simicević, Nucl. Phys. A **534**, 541 (1991).
[8] F. Adimi, H. Breuer, B. S. Flanders, M. A. Khandaker, M. G. Khayat, P. G. Roos, D. Zhang, Th. S. Bauer, J. Konijn, C. T. A. M. de Laat, G. S. Kyle, S. Mukhopadhyay, M. Wang, and R. Tacik, Phys. Rev. C **45**, 2589 (1992).
[9] O. A. Zaimidoroga, M. M. Kulyukin, R. M. Sulyaev, I. V. Falomkin, A. I. Filippov, V. M. Tsupko-Sitnikov, and Yu. A. Shcherbakov, Sov. Phys. JETP **21**, 848 (1965); **24**, 1111 (1967).
[10] J. McCarthy, T. Meyer, R. C. Minehart, E. A. Wadlinger, K. O. H. Ziock, and J. Vincent, Phys. Rev. C **11**, 266 (1975).
[11] D. Gotta, M. Dörr, W. Fetscher, G. Schmidt, H. Ullrich, G. Backenstoss, W. Kowald, I. Schwanner, and H.-J. Weyer, Phys. Lett. **112B**, 129 (1982).
[12] P. Truöl, H. W. Baer, J. A. Bistirlich, K. M. Crowe, N. de Botton, and J. A. Helland, Phys. Rev. Lett. **32**, 1268 (1974).
[13] A. V. Bannikov, B. Levay, V. I. Petrukhin, V. A. Vasilyev, L. M. Kochenda, A. Markov, V. I. Medvedev, G. L. Sokolov, I. I. Strakovsky, and D. Horváth, Nucl. Phys. A **403**, 515 (1983).
[14] F. Corriveau, M. D. Hasinoff, D. F. Measday, J.-M. Poutissou, and M. Salomon, Nucl. Phys. A **473**, 747 (1987).
[15] G. Backenstoss, M. Izycki, P. Salvisberg, M. Steinacher, P. Weber, H. J. Weyer, S. Cierjacks, S. Ljungfelt, H. Ullrich, M. Furić, and T. Petković, Phys. Rev. Lett. **55**, 2782 (1985).
[16] K. A. Aniol, A. Altman, R. R. Johnson, H. W. Roser, R. Tacik, U. Wienands, D. Ashery, J. Alster, M. A. Moinester, E. Piasetzky, D. R. Gill, and J. Vincent, Phys. Rev. C **33**, 1714 (1986).
[17] L. C. Smith, R. C. Minehart, D. Ashery, E. Piasetzky, M. Moinester, I. Navon, D. F. Geesaman, J. P. Schiffer, G. Stephens, B. Zeidman, S. Levinson, S. Mukhopadhyay, R. E. Segel, B. Anderson, R. Madey, J. Watson, and R. R. Whitney, Phys. Rev. C **40**, 1347 (1989).
[18] R. A. Cecil, B. D. Anderson, and R. Madey, Nucl. Instrum. Methods **161**, 439 (1979).
[19] T. J. Gooding and H. G. Pugh, Nucl. Instrum. Methods **7**, 189 (1960).
[20] D. L. Smith, R. G. Polk, and T. G. Miller, Nucl. Instrum. Methods **64**, 157 (1968).
[21] D. Gotta, KFK Report 3226, 1981.
[22] W. Kowald, Ph.D. thesis, University of Basel, 1981.
[23] D. F. Measday and C. Richard-Serre, Nucl. Instrum. Methods **76**, 45 (1969).
[24] B. Bassalleck, W.-D. Klotz, F. Takeuchi, H. Ullrich, and M. Furić, Phys. Rev. C **16**, 1526 (1977).
[25] R. J. Kurz, Lawrence Radiation Laboratory Report UCRL-11339,1964.
[26] S. A. Elbakr, J. W. Watson, and C. A. Miller, Nucl. Instrum. Methods **115**, 115 (1974).
[27] S. Cierjacks, T. Petković, H. Ullrich, D. Gotta, S. Ljungfelt, N. Simicević, M. Izycki, P. Weber, and H.-J. Weyer, Nucl. Instrum. Methods A **238**, 354 (1985).
[28] G. Backenstoss, M. Izycki, W. Kowald, P. Weber, H.-J. Weyer, S. Ljungfelt, U. Mankin, G. Schmidt, and H. Ullrich, Nucl. Phys. A **448**, 567 (1986).
[29] G. Backenstoss, W. Kowald, I. Schwanner, H. -J Weyer, M. Dörr, D. Gotta, G. Schmidt, L. M. Simons, and H. Ullrich, Phys. Lett. **115B**, 445 (1982).
[30] D. Gotta and H.-J. Weyer, program ONLMNG, unpublished.
[31] E. Jans, P. Barreau, M. Bernheim, J. M. Finn, J. Morgenstern, J. Mougey, D. Tarnowsky, S. Turck-Chieze, S. Frullani, F. Garibaldi, G. P. Capitani, E. de Sanctis, M. K. Brussel, and I. Sick, Phys. Rev. Lett. **49**, 974 (1982).
[32] E. Jans, M. Bernheim, M. K. Brussel, G. P. Capitani, E. de Sanctis, S. Frullani, F. Garibaldi, J. Morgenstern, J. Mougey, I. Sick, and S. Turck-Chieze, Nucl. Phys. A **475**, 687 (1987).
[33] P. Weber, G. Backenstoss, M. Izycki, R. J. Powers, P. Salvisberg, M. Steinacher, H. J. Weyer, S Cierjacks, A. Hoffart, H. Ullrich, M. Furić, T. Petković, and N. Simicević, Nucl. Phys. A **501**, 765 (1989).
[34] G. F. Krebs, C. Cox, J. M. Daniels, T. Gajdicar, P. Kirkby, and A. D. May, Nucl. Phys. A **395**, 364 (1983).
[35] D. S. Koltun, Phys. Rev. **162**, 963 (1967).
[36] E. Byckling and E. Kajantie, *Particle Kinematics* (Wiley, London, 1973), Chap. V.
[37] M. C. Goldberger and K. M. Watson, *Collision Theory* (Wiley, New York, 1964), p. 549.
[38] H. Nägeli, Ph.D. thesis, University of Basel, 1980.
[39] H. Brückmann, W. Kluge, H. Matthäy, L. Schänzler, and K. Wick, Nucl. Phys. A **157**, 209 (1970).
[40] B. Zeitnitz, R. Maschuw, and P. Suhr, Nucl. Phys. A **149**, 449 (1970).
[41] J. Reich, Diploma work, University of Karlsruhe, 1983, unpublished.
[42] I. Schwanner, G. Backenstoss, W. Kowald, L. Tauscher, H.-J. Weyer, D. Gotta, and H. Ullrich, Nucl. Phys. A **412**, 253 (1984).
[43] A. J. Rusi el Hassani, ETH Zürich Report No. 9256, 1990.
[44] R. Landua, Ph.D. thesis, University of Mainz, 1980.
[45] R. Landua and E. Klempt, Phys. Rev. Lett. **48**, 1722 (1982).
[46] Y. Eisenberg and D. Kessler, Nuovo Cimento **19**, 1195 (1961).
[47] A. C. Phillips and F. Roig, Nucl. Phys. A **234**, 378 (1974).
[48] R. Sachs, *Nuclear Theory* (Cambridge University Press, Cambridge, 1953).
[49] R. Mach, Nucl. Phys. A **258**, 513 (1976).
[50] K. A. Brueckner, R. Serber, and K. M. Watson, Phys. Rev. **84**, 258 (1951).
[51] A. M. L. Messiah, Phys. Rev. **87**, 639 (1952).
[52] I. T. Cheon, Phys. Rev. **145**, 794 (1966).
[53] L. Tauscher and W. Schneider, Z. Phys. **271**, 409 (1974).
[54] C. J. Batty, E. Friedman, and A. Gal, Nucl. Phys. A **402**, 411 (1983).
[55] R. Seki and K. Masutani, Phys. Rev. C **27**, 2799 (1983).
[56] J. Konijn, C. T. A. M. de Laat, A. Taal, and J. H. Koch, Nucl. Phys. A **519**, 773 (1990).
[57] M. Ericson and T. E. O. Ericson, Ann. Phys. (N.Y.) **36**, 323 (1966).
[58] M. Krell and T. E. O. Ericson, Nucl. Phys. B **11**, 521 (1969).

[59] S. G. Eckstein, Phys. Rev. **129**, 413 (1963).
[60] P. P. Divakaran, Phys. Rev. **139**, B387 (1965).
[61] C. Pajares and R. Pascual, Nucl. Phys. B **35**, 631 (1971).
[62] J. Roginsky and C. Werntz, Phys. Rev. C **40**, 2732 (1989).
[63] A. Figureau and M. Ericson, Nucl. Phys. B **10**, 349 (1969).
[64] A. C. Phillips and F. Roig, Nucl. Phys. B **60**, 93 (1973).
[65] H. O. Meyer, M. A. Ross, R. E. Pollock, A. Berdoz, F. Dohrmann, J. E. Goodwin, M. G. Minty, H. Nann, P. V. Pancella, S. F. Pate, B. V. Przewoski, T. Rinckel, and F. Sperisen, Phys. Rev. Lett. **65**, 2846 (1990).
[66] D. A. Hutcheon, E. Korkmaz, G. A. Moss, R. Abegg, N. E. Davison, G. W. R. Edwards, L. G. Greeniaus, D. Mack, C. A. Miller, W. C. Olsen, I. J. van Heerden, and Y. E. Yanlin, Nucl. Phys. A **535**, 618 (1991).
[67] B. G. Ritchie, R. C. Minehart, T. D. Averett, G. S. Blanpied, K. Giovanetti, B. M. Preedom, D. Rothenberger, L. S. Smith, and J. R. Tinsley, Phys. Rev. Lett. **66**, 568 (1991).
[68] J.-F. Germond and C. Wilkin, J. Phys. G **14**, 181 (1988).
[69] B. K. Jain, Nucl. Phys. A **296**, 479 (1978).
[70] C. M. Rose, Phys. Rev. **154**, 1305 (1967).
[71] C. Kerboul, A. Boudard, L. Antonuk, J. Arvieux, J. Berger, R. Bertini, M. Boivin, J. M. Durand, A. Stetz, J. Tinsley, J. Yonnet, Nguyen van Sen, Ye Yanlin, B. Mayer, J. Cameron, C. Lapointe, D. M. Sheppard, J. F. Germond, and C. Wilkin, Phys. Lett. B **181**, 28 (1986).
[72] A. Boudard, C. Kerboul, L. Antonuk, J. Arvieux, J. Berger, R. Bertini, M. Boivin, J. M. Durand, G. Roy, J. Tinsley, J. Yonnet, B. Mayer, and Nguyen van Sen, Phys. Lett. B **214**, 6 (1988).
[73] M. Brack, D. O. Riska, and W. Weise, Nucl. Phys. A **287**, 425 (1977).
[74] G. F. Bertsch and D. O. Riska, Phys. Rev. C **18**, 317 (1978).
[75] O. V. Maxwell, W. Weise, and M. Brack, Nucl. Phys. A **348**, 388 (1980).
[76] K. Shimizu, A. Faessler, and H. Müther, Nucl. Phys. A **343**, 468 (1980).
[77] D. S. Koltun and S. Reitan, Phys. Rev. **141**, 1413 (1966).
[78] D. S. Koltun and S. Reitan, Nucl. Phys. B **4**, 629 (1968).
[79] F. Hachenberg, J. Hüfner, and H. J. Pirner, Phys. Lett. **66B**, 425 (1977).
[80] F. Hachenberg and J. Pirner, Ann. Phys. (N.Y.) **112**, 401 (1978).
[81] A. W. Thomas and R. H. Landau, Phys. Rep. **58**, 121 (1980).
[82] V. P. Efrosinin, D. A. Zaikin, and I. I. Osipchuk, Z. Phys. A **328**, 315 (1987).
[83] J. Chai and D. O. Riska, Phys. Rev. C **19**, 1425 (1979).
[84] D. O. Riska and H. Sarafian, Phys. Lett. **95B**, 185 (1980).
[85] K. Shimizu and A. Faessler, Nucl. Phys. A **333**, 495 (1980).
[86] L. L. Kiang, T.-S.H. Lee, and D. Riska, Phys. Rev. C 50,2703 (1994).
[87] T.-S. H. Lee and D. O. Riska, Arognne National Laboratory report, 1992.
[88] T.-S. H. Lee and K. Ohta, Phys. Rev. Lett. **49**, 1079 (1982).
[89] H. Toki and H. Sarafian, Phys. Lett. **119B**, 285 (1982).
[90] R. R. Silbar and E. Piasetzky, Phys. Rev. C **29**, 1116 (1984); **30**, E1365 (1984).
[91] K. Otha, M. Thies, and T.-S. H. Lee, Ann. Phys. (N.Y.) **163**, 420 (1985).
[92] O. V. Maxwell and C. Y. Cheung, Nucl. Phys. A **454**, 606 (1986).
[93] M. A. Pickar, A. D. Bacher, H. O. Meyer, R. E. Pollock, and G. T. Emery, Phys. Rev. C **46**, 397 (1992).
[94] J. N. Ginnocchio, Phys. Rev. C **17**, 195 (1978).
[95] J. A. Niskanen, Phys. Rev. C **43**, 36 (1991).
[96] G. Audit, A. Bloch, N. d'Hose, L. Jammes, J. Laget, J. Martin, C. Schahl, G. Tamas, C. Sun, C. F. Perdrisat, L. Ghedira, D. Ben-Meir, M. Rodgers, L. Murphy, P. Stoler, P. Argan, and P. Pedroni, Phys. Lett. B **227**, 331 (1989).
[97] J. A. Niskanen, Phys. Lett. B **289**, 227 (1992).
[98] M. Dörr, W. Fetscher, D. Gotta, J. Reich, H. Ullrich, G. Backenstoss, W. Kowald, and H. J. Weyer, Nucl. Phys. A **445**, 557 (1985).
[99] P. Weber, J. McAlister, R. Olszewski, A. Feltham, M. Hanna, D. Humphrey, R. R. Johnson, G. J. Lolos, Y. Mardor, S. May-Tal, D. Ottewell, Z. Papandreou, M. Pavan, C. Ponting, F. M. Rozon, M. Sevior, G. Sheffer, G. R. Smith, V. Sossi, R. Tacik, and D. Vetterli, Phys. Lett. B **233**, 281 (1989); Phys. Rev. C **43**, 1553 (1991).
[100] E. Daum, St. Vinzelberg, D. Gotta, H. Ullrich, G. Backenstoss, P. Weber, H. J. Weyer, M. Furić, and T. Petković, in preparation.
[101] R. D. McKeown, S. J. Sanders, J. P. Schiffer, H. E. Jackson, M. Paul, J. R. Specht, E. J. Stephenson, R. P. Redwine, and R. E. Segel, Phys. Rev. Lett. **44**, 1033 (1980).
[102] H. Yokota, T. Mori, T. Katsumi, S. Igarashi, K. Hama, R. Chiba, K. Nakai, J. Chiba, H. En'yo, S. Sasaki, T. Nagae, and M. Sekimoto, Phys. Rev. Lett. **58**, 191 (1987).
[103] B. Bassalleck, H.-D. Engelhardt, W.-D. Klotz, F. Takeuchi, H. Ullrich, and M. Furić, Nucl. Phys. A **319**, 397 (1979).
[104] B. Coupat, P. Bertin, and D. Isabelle, Nucl. Phys. A **403**, 497 (1983).